AGU PUBLICATIONS

JGR

Journal of Geophysical Research: Solid Earth

RESEARCH ARTICLE
10.1002/2016JB013337

Key Points:
- High-resolution structural image of underthrusting Indian lithosphere and orogenic wedge enhanced by 3-D receiver function migration
- Crustal-scale listric deformation structures beneath the Main Himalayan Thrust
- Along-strike variations in the collision structure across Bhutan driven by large-scale lithosphere slab dynamics

Supporting Information:
- Supporting Information S1

Correspondence to:
J. Singer,
julia.singer@erdw.ethz.ch

Citation:
Singer, J., E. Kissling, T. Diehl, and G. Hetényi (2017), The underthrusting Indian crust and its role in collision dynamics of the Eastern Himalaya in Bhutan: Insights from receiver function imaging, *J. Geophys. Res. Solid Earth*, *122*, 1152–1178, doi:10.1002/2016JB013337.

Received 6 JUL 2016
Accepted 21 DEC 2016
Accepted article online 24 DEC 2016
Published online 3 FEB 2017

The underthrusting Indian crust and its role in collision dynamics of the Eastern Himalaya in Bhutan: Insights from receiver function imaging

J. Singer[1], E. Kissling[1], T. Diehl[2], and G. Hetényi[1,2,3]

[1]Institute of Geophysics, Swiss Federal Institute of Technology, ETH Zurich, Zurich, Switzerland, [2]Swiss Seismological Service, ETH Zurich, Zurich, Switzerland, [3]Now at Institute of Earth Sciences, University of Lausanne, Lausanne, Switzerland

Abstract Most of the convergence rate between the Indian and Eurasian plate is assumed to be absorbed along a major basal thrust beneath the Himalaya, the Main Himalayan Thrust (MHT). Deformation along this basal thrust in combination with frontal accretion results in the formation of the upper crustal fold-thrust belt. The role of the underthrusting Indian crust and its impact on the long-term growth of the Himalaya are only poorly understood, partly due to the lack of high-resolution seismic images of the crust. To improve the imaging of lithospheric structures, we developed a 3-D migration scheme for receiver functions using seismic data from the temporary GANSSER network in Bhutan. Extending the 2-D high-frequency ray approximation and common conversion point stacking to 3-D including linear phase weighting and a quality assessment, we reveal significant along-strike differences in the lithospheric structure beneath Bhutan. In western Bhutan, the Moho geometry shows an increased dip south of the Higher Himalaya reaching almost 70 km depth thereafter, whereas in eastern Bhutan the Moho is almost subhorizontal at 50 km depth across our network. The appearance of distinct listric structures beneath the MHT indicates intracrustal deformation up to crustal imbrication down to the lower crust. We propose that these variations, in the crustal thickness and in intracrustal structures, influence the upper crustal kinematics of the Bhutan Himalayan orogeny and are primarily driven by an Indian mantle-slab northwest of Bhutan, and its absence northeast of Bhutan.

1. Introduction

In an active continental collision the accumulation of strain is a combination of frontal accretion in the upper crust, deformation in the underthrusting continental plate, and the formation of an upper crustal fold-thrust belt, like the Himalayan orogenic wedge [*Avouac*, 2003, 2007]. The tectonic process of crustal accretion in orogenic collisions is often reduced to the frontal accretion of upper crustal material from the underthrusting plate, neglecting crustal imbrication of the underthrusting crust and its involvement in the long-term growth of the mountain belt. However, to sustain the long-term growth and uplift of mountain belts over tens of millions of years an involvement of the underthrusting crust in the deformation is needed.

Recent studies in the Himalaya focusing on the crustal deformation and exhumation history of the fold-thrust belt [*Herman et al.*, 2010; *Grandin et al.*, 2012; *Avouac*, 2007; *van der Beek et al.*, 2016] propose such an involvement of the underthrusting basement in the kinematics of the orogenic wedge. An involvement of the underthrusting basement provides an explanation for higher exhumation rates at the front of the Higher Himalaya in correlation with an abrupt rise in topography, and the long-term growth of the Himalayan orogenic wedge over the last 11 Ma by the development of a fold-thrust belt including the growth of duplex structures in the Lesser Himalaya [*DeCelles et al.*, 2001; *Long et al.*, 2011a]. In these models the involvement of the underthrusting crust is in general limited to a crustal imbrication process at middle crustal depth, whereby parts of the underthrusting material is imbricated to the overlying orogenic wedge beneath the Higher Himalaya. Direct evidence for such tectonic processes and structures are still missing and are not reflected in seismic images of the Himalaya, neither by receiver function images [e.g., *Schulte-Pelkum et al.*, 2005; *Nabelek et al.*, 2009; *Acton et al.*, 2011; *Caldwell et al.*, 2013] nor in images of seismic velocity anomalies [e.g., *Monsalve et al.*, 2008; *Huang et al.*, 2009; *Guo et al.*, 2009; *Sheehan et al.*, 2014]. Evidence for ductile deformation in the middle to lower crust, leading to significant strain accumulation, have been so far provided by

strong anisotropic receiver function signals in the northern part of the Himalayan orogenic wedge beneath the Higher and Tethyan Himalaya in eastern Nepal [*Schulte-Pelkum et al.*, 2005].

In other active collision zones like the Taiwan orogen, however, seismic images of the underthrusting crust indicate strong lower crustal anisotropy, which is interpreted as the result of an imbrication process in the middle and lower crust, induced by the motion of underthrusting basement [*Huang et al.*, 2015].

Along the Himalayan collision belt, the lithospheric structure of the Eastern Himalaya in the region of Bhutan is only poorly constrained by seismological studies despite its particular structural and tectonic setting in the Himalayan arc: south of the Bhutan Himalaya the Shillong Plateau presents a unique Himalayan foreland basement uplift with recent exhumation during the Pliocene [*Biswas et al.*, 2007; *Najman et al.*, 2016], to the west the region is bounded by the tectonic high-relief Tista window in Sikkim and toward the east the transition zone to the Eastern Himalayan syntaxis begins with the Arunachal Pradesh.

To provide the first detailed seismic images of the lithospheric structure in this region, we deployed a temporary seismic network across Bhutan, the Geodynamics ANd Seismic Structure of the Eastern Himalaya Region (GANSSER) network. We image the lithospheric collision structure across two densely spaced arrays in eastern and western Bhutan by using the intrinsic sensitivity of receiver functions to first-order seismic discontinuities. Seismic discontinuities can be first-order changes in shear wave velocities due to compositional differences or tectonic deformation zones with distinct *P* wave anisotropy. Converted phases, generated at such interfaces, are isolated by the receiver function analysis and are used to image the crustal structure beneath a seismic station or array. In complex tectonic regions, as expected for the orogenic collision zone in the Bhutan Himalaya, variable dipping interfaces and appearance of multiples in receiver functions can lead to distorted interfaces and/or the appearance of artifacts in migration images without applying an accurate imaging approach.

In this study, we introduce a 3-D receiver function migration approach following the method of *Abe et al.* [2011] to reduce migration artifacts and to improve the accuracy in imaging dipping seismic conversion structures with 2-D seismic arrays. For the receiver function imaging we use teleseismic earthquakes recorded with the temporary GANSSER network in Bhutan. First, we assess the Moho geometry of the underthrusting Indian crust and discuss lateral variations between eastern and western Bhutan in relation to the large-scale lithospheric structure of the Indian-Eurasian collision. In combination with the local seismicity, we identify predominant intracrustal structures in the underthrusting Indian crust. Finally, we discuss the influence of these structures on the deformation kinematics in the Bhutan Himalaya and its relation to the variation in the Moho geometry and the large-scale collision structure in this region.

2. Tectonic Setting of the Himalayan Orogen in Bhutan

The Bhutan Himalaya is located in the Eastern Himalaya, between the deeply incised high-relief Tista window in Sikkim and Arunachal Pradesh in the west (Figure 1). Characteristics for the Himalayan fold-and-thrust belt in Bhutan are klippen of the Tethyan sedimentary sequence, consisting of metasediments preserved on top of the Great Himalaya Sequence [e.g., *Kellett et al.*, 2009]. The formation of tectonic windows exposing the younger accreted Lesser Himalaya Sequence beneath the high-grade metamorphic Greater Himalaya Sequence is less pronounced compared to Sikkim and Nepal but is present in the Paro window in western Bhutan or the Kuru Chu half-window in eastern Bhutan (Figure 1). South of Bhutan, the presence of the Shillong plateau, a young foreland basement uplift, exhumed during the Pliocene with a present-day average elevation of 1600 m, marks a unique foreland structure along the Himalayan arc. Its western end is at 90°E and the eastern end extends beyond eastern Bhutan to the foreland of Arunachal Pradesh. Whether and how this foreland uplift influences the tectonic or erosion rates of the Eastern Himalaya is still a matter of debate [*Bilham and England*, 2001; *Biswas et al.*, 2007; *Clark and Bilham*, 2008; *Banerjee et al.*, 2008]. Another characteristic of the Bhutan Himalaya is the relatively thin sedimentary cover of up to 1 km in the Brahmaputra valley, where Indian basement outcrops just 50 km from the southern front of the Himalaya [*Dasgupta et al.*, 2000]. In other regions of the Indian foreland, like in the Central Himalayas, the sedimentary basin in the foredeep has an average thickness of 4 km [*Dasgupta et al.*, 2000].

Besides these structural and geomorphological characteristics, the region of Bhutan features an apparently lower seismicity in comparison to neighboring regions like Sikkim and Arunachal Pradesh [*Gahalaut et al.*, 2011]. This implies either a strong interseismic coupling along the Main Himalayan Thrust, a lower rate of brittle deformation, or lower strain rates in the Bhutan Himalaya. However, based on geodetic measurements,

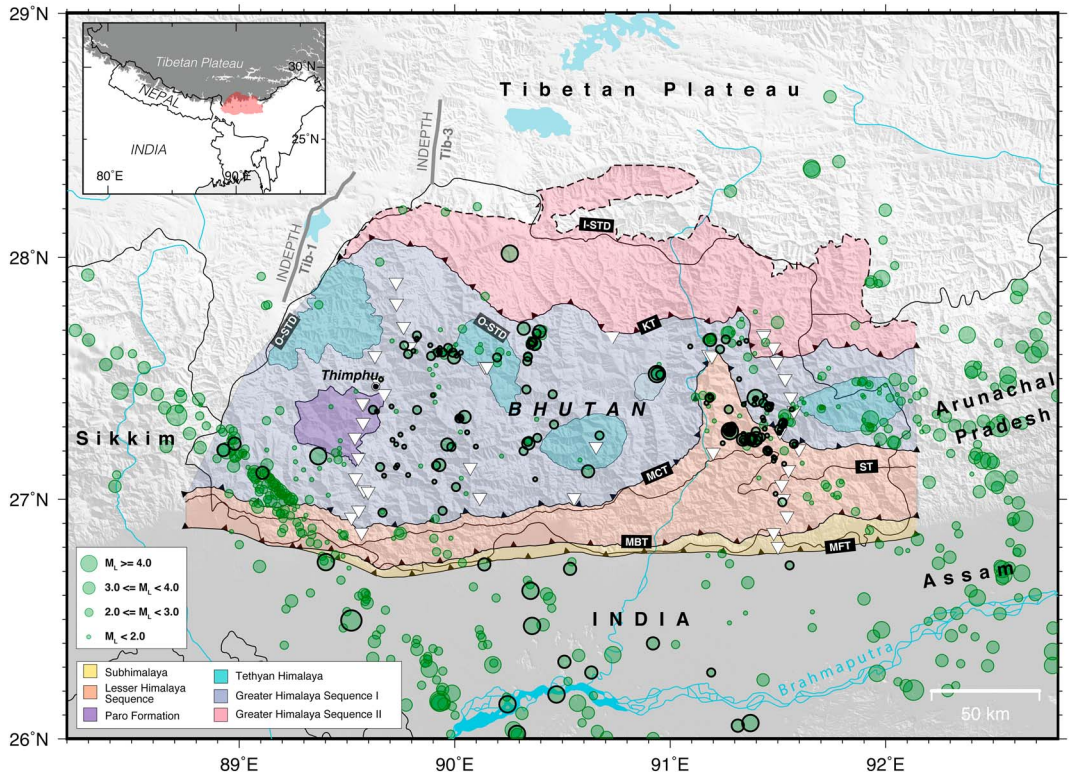

Figure 1. Tectonic map of the Bhutan Himalaya. Seismic stations of the temporary GANSSER network are shown by white triangles. Green circles represent local earthquakes recorded by the GANSSER network between January 2013 and November 2014. Well-constrained hypocenter locations of events with maximum azimuthal gap without observation (GAP) <200° and ≥10 phase observations are shown with black contour. Main lithotectonic units are colored according to *Long et al.* [2011b]. MFT, Main Frontal Thrust; MBT, Main Boundary Thrust; MCT, Main Central Thrust; KT, Kakhtang Thrust; I-STD, internal South Tibetan detachment; O-STD, outer South Tibetan detachment; ST, Shumar Thrust. The gray thick lines, northwest of Bhutan indicate the location of the wide-angle reflection profiles, Tib-1 and Tib-3 of the INDEPTH project [e.g., *Hauck et al.*, 1998].

the average present-day convergence rate across the Bhutan Himalaya of 14–17 mm/yr differs not significantly to the surrounding regions [*Vernant et al.*, 2014] and precludes a lower strain rate. Additional evidence for along-strike differences come from multithermochronologic data, which suggest nonuniform exhumation rates between eastern and western Bhutan [*Coutand et al.*, 2014] and indicate variations in the upper crustal structure and geometry of the main detachment thrust.

Like in other parts of the Himalaya, the frontal orogenic structure in Bhutan is characterized by fold-thrust systems in its southernmost part, the Subhimalaya. It is a foreland fold-and-thrust belt [e.g., *Hirschmiller et al.*, 2014], which includes unmetamorphosed Siwalik sediments, the molasse deposits of upper Miocene to Quaternary age [*Landry et al.*, 2016]. Sedimentary material from the uppermost part of the Indian crust, deposited on the northern margin of the Indian Plate during Paleo-Proterozoic to Paleozoic [e.g., *Schelling and Arita*, 1991] was scraped off and accreted to the Himalayan orogenic wedge by southward progression of the frontal listric thrust fault. The Subhimalayas were overthrusted along the Main Boundary Thrust (MBT) by greenschist-facies metasedimentary rocks of the Lesser Himalayan Sequence (LHS) [*Gansser*, 1983]. These rocks are deformed in a series of duplexes, whose geometry rapidly varies along strike [*Long et al.*, 2011a]. The LHS is overthrusted by high-metamorphic grade rocks of the Greater Himalaya Sequence (GHS) in the central and northern parts of the Himalaya. The thrusting occurred in southward direction until at least 13 Ma ago [*Daniel et al.*, 2003; *Tobgay et al.*, 2012] along the Main Central Thrust (MCT), one of the main thrust faults in the Himalaya collision structure. Similar to the more recently active Main Boundary Thrust (MBT) and the currently active Main Frontal Thrust (MFT) in the south, these thrust faults are assumed to merge as listric faults with the Main Himalayan Thrust (MHT) at depth. The MHT is the predominant intracrustal collision structure in the Himalaya orogen, which separates the underthrusting Indian plate from the overlying upper crustal fold-thrust belt [*Argand*, 1924; *Gansser*, 1964; *Nelson et al.*, 1996].

3. The GANSSER Experiment

For the GANSSER experiment, we deployed a temporary seismic network in Bhutan between January 2013 and November 2014. The network consists of 38 three-component broadband seismometers (24 Streckeisen STS2 and 14 Nanometrics Trillium Compact) with two densely spaced south-north arrays across the Himalayan orogenic wedge in western and eastern Bhutan, reaching from the Subhimalaya foothills north of the Brahmaputra valley toward the South Tibetan Detachment (STD) zone in the Great Himalayan Sequence, and eight additional stations in central Bhutan (Figure 1).

To allow for a continuous imaging of the crustal structure with overlapping receiver function information from neighboring stations, we chose an interstation spacing of 7–8 km along both south-north arrays and used stations in the center mainly for the detection and location of local earthquakes. The data were continuously recorded with a sampling frequency of 100 Hz. For the first 15 months we ran the entire network with 38 stations and afterward it was reduced to a 14 station network with the primary goal to record local seismicity for the last 7 months. Additionally, stations from China (in Lhasa, station LSA) and India (on the Shillong Plateau, station SHL and in Sikkim) are used to improve the accuracy in hypocenter location of selected earthquakes, which are located outside of the GANSSER network.

4. Method

4.1. Teleseismic Data and Receiver Function Calculation

We calculated radial and transverse *P*-to-*S* receiver functions (RF) from teleseismic *P* and *PP* arrivals using the iterative time domain deconvolution method following *Ligorría and Ammon* [1999]. For RF calculations from converted *P* arrivals we first select earthquakes within an epicentral distance 25–95° and magnitude $m_b \geq 5.2$, and from *PP* arrivals, earthquakes within epicentral distance 145–170° and magnitude $m_b \geq 6.2$.

The teleseismic signal is cut 30 s prior and 160 s after the predicted *P* phase, respectively, *PP* phase, arrival using a global 1-D velocity model (IASPEI91 [*Kennett and Engdahl*, 1991]). Subsequently, we transform the vertical-north-east (Z-N-E) seismograms to a vertical-radial-transverse system (Z-R-T) based on the event back azimuth. By this rotation, we separate the incident wave field (*P* or *PP*) from the converted *Ps* phases on the radial component in a first-order approximation. Prior to the deconvolution of the *R* and *T* seismograms with the *Z* component, we apply the following preprocessing to allow an efficient and stable receiver function calculation: downsampling (10 Hz), detrending, tapering (Hanning window filter), and band-pass filtering (0.08–0.8 Hz with a second-order Butterworth filter). For the iterative time domain deconvolution, we use a Gaussian filter parameter of 4 (corresponding to a pulse width of 1.25 s, equivalent to 0.8 Hz low-pass filter) to suppress high-frequency noise in the RF signal.

To obtain a high-quality data set, we apply an automatic quality selection to all radial and transverse RF. Only RF that match the following criteria are retained for the migration: an impulsive *P* phase arrival on the initial vertical (*Z*) component (signal-to-noise ratio larger than 3), minimum variance reduction of 70% during deconvolution (as described by *Ligorría and Ammon* [1999]), a maximum positive amplitude of 1.0 for the direct RF *P* phase arrival (only applied to the radial RFs) [*Schulte-Pelkum and Mahan*, 2014a], an absolute noise amplitude within 5 s prior to the direct RF *P* phase arrival less than 40% of the maximum RF amplitude (similar to *Hetényi et al.* [2015]), a maximum positive amplitude of the direct *P* phase within ±0.5 s zero lag time, any arrival pulses smaller than twice the direct *P* phase arrival amplitude (only applied to the radial RFs), and any arrival pulse width of the RF signal less than 3.5 s. Our final RF data set consists of 1704 RF functions for the western array and 1429 for the eastern array shown in Figure 2. For the 3-D migration, we normalize all receiver function signals with the average *P* phase amplitude arrival of all radial RFs of each array. This normalization retains variable phase arrival intensities due to 3-D effects of phase conversions and variations in epicentral distances as indicated for example by the radial RFs of station BHE05 in Figure 3.

4.2. Preliminary Constraints on Moho Depth From Individual Stations

For a priori constraints on the general lithospheric structure along the two arrays, we started with a time-to-depth conversion of RFs for individual stations following the H-κ method of *Zhu and Kanamori* [2000].

We use a minimum 1-D *P* and *S* wave velocity model (Figure 4), derived from local earthquake data as an independent information on the first-order crustal velocities in Bhutan to confine v_P/v_S ranges in the H-κ grid search. The so-called *minimum* 1-D velocity model for Bhutan (Figure 4) is derived by solving the coupled

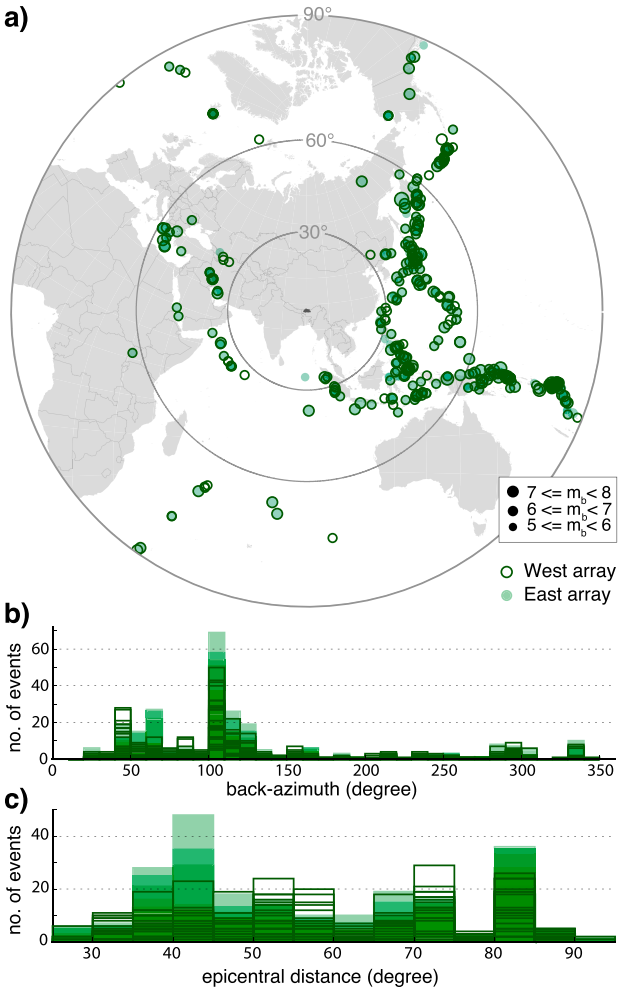

Figure 2. (a) Distribution of the teleseismic earthquake data set used to compute *P*-to-*S* receiver function and 3-D time-to-depth migration. The data set contains teleseismic events with $m_b > 5.2$, which occurred between January 2013 and November 2014. (b) Back azimuth distribution of individual stations along the eastern (green solid) and western (green outline) arrays. (c) Distribution of epicentral distance of individual stations along the eastern (green solid) and western (green outline) arrays.

hypocenter-velocity problem with the program VELEST [*Kissling*, 1988] for well-locatable local earthquakes recorded by the GANSSER network (see Text S1 and Figure S1 in the supporting information). This type of 1-D velocity model yields a global minimum data fit and represents the average 1-D velocity structure of a region.

In this study, we neglect lateral variations in crustal velocities between eastern and western Bhutan for the RF migration due to the lack of a homogeneously resolved 3-D crustal *P* and *S* wave velocity model. Although station corrections in the minimum 1-D velocity model seem to indicate such an east-west variation (Figure S1 in the supporting information), the consideration of poorly constrained local velocity variations would introduce an additional ambiguity in the time-to-depth migration results.

In the raw RF signal or modified H-κ grid search approach (Figure S2 in the supporting information) no distinct Moho multiples can be identified, likely due to attenuation and scattering of multiples at intracrustal discontinuities which can interfere with direct Moho conversion signals. As a consequence, we focus only on direct *Ps* phases and neglected multiples in our analysis. For the depth (H) and v_P/v_S (κ) grid search an average crustal *P* wave velocity of 6.15 km/s is used with three depth-dependent v_P/v_S ranges (1.66–1.68 from 0 to 20 km depth, 1.67–1.70 from 20 to 40 km and 1.69–1.71 from 40 to 80 km depth) based on the results of the minimum 1-D velocity models to constrain the depth of *P*-to-*S* RF signals.

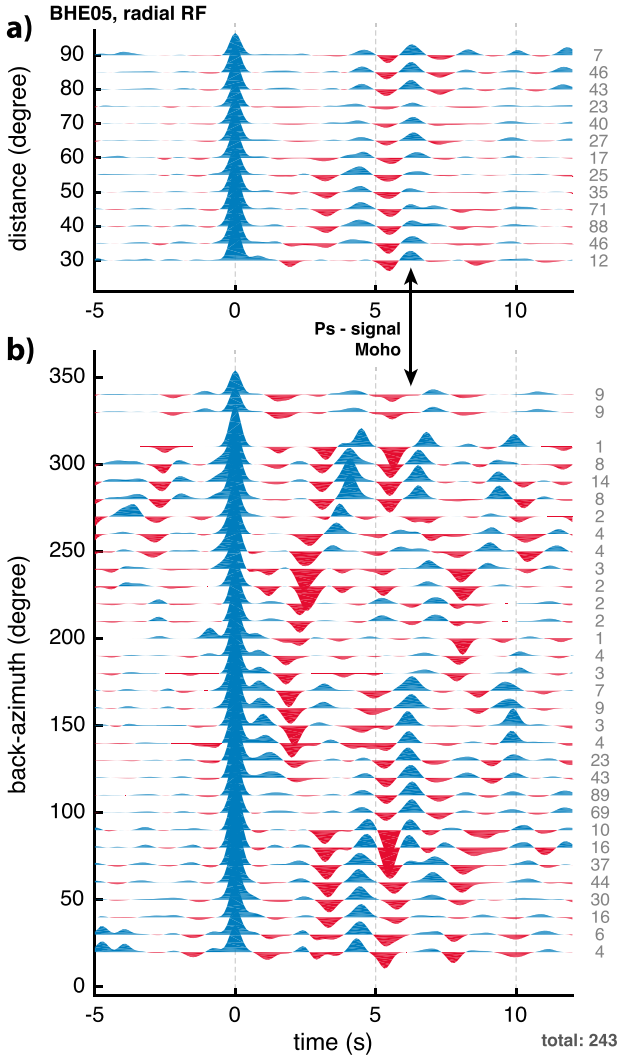

Figure 3. Example of high variability in phase conversion signals in radial *P*-to-*S* receiver functions with back azimuth for one station (BHE05 along the eastern array located at 91.5183°E/27.060°N). Receiver functions are stacked in (a) 5° bins with 2.5° overlap for the epicentral distance and (b) 10° bins with 5° overlap for the back azimuthal distribution. Numbers on the right indicate the number of traces stacked in each bin. Initial radial and vertical component are band-pass filtered between 0.08 and 0.8 Hz before deconvolution.

Results from this single-station time-to-depth conversion of radial and transverse RF signals indicate multiple intracrustal discontinuities with a generally northward dipping orientation (Figure S3 in the supporting information). The Indian Moho appears to enter the Himalayan orogen beneath the MFT at around 45–50 km depth in eastern and western Bhutan and deepens to at least 62 km depth at ~130 km distance from the MFT in western Bhutan (Figure S3a in the supporting information). Beneath the eastern array the simple time-depth migration results reveal instead a rather uniform low-angle northward dipping of the Moho (Figure S3b in the supporting information).

4.3. Iterative 3-D Receiver Function Migration

For the time-to-depth migration of RF we apply a method which allows to image complex and dipping seismic discontinuities, as well as lateral variations of these structures with an 2-D seismic array and a strongly heterogeneous back azimuth coverage of data, with out-of-plane ray geometries.

A range of methodologies has been developed to back propagate converted teleseismic wave fields to specific points in space, mainly in 2-D with isotropic 1-D velocity models [e.g., *Dueker and Sheehan*, 1998; *Kosarev*, 1999] assuming planar teleseismic wavefronts with constant ray parameters. The assumption of

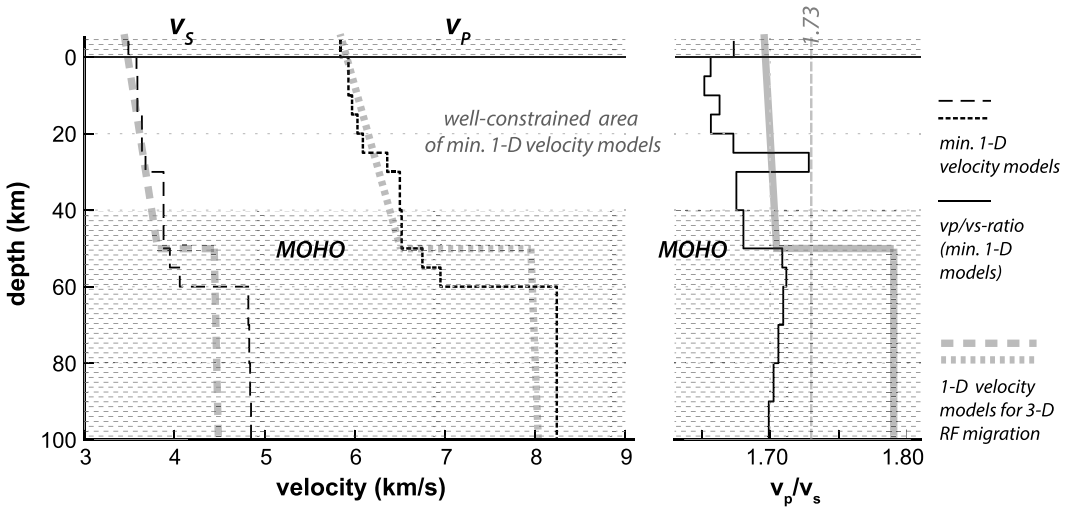

Figure 4. *P* and *S* wave velocity gradients for 3-D receiver function migration (thick gray lines) based on local minimum 1-D *P* and *S* wave velocity models (thin black lines). The separately derived minimum 1-D *P* and *S* wave velocity model are based on earthquakes recorded by the GANSSER network in Bhutan and surrounding regions (more details in Text S1 and Figure S1 in the supporting information). For the *S* wave model, hypocenter locations were fixed, which were initially defined by the *P* wave model to reduce the number of unknowns with less *S* wave phase observations (see Figure S1 in the supporting information). For the 3-D migration of the RFs a constant crustal velocity gradient of 0.0118 s^{-1} for the *P* wave velocities and a gradient of 0.0067 s^{-1} for *S* wave velocities is defined, respectively. For the mantle, a constant velocity gradient of 0.0016 s^{-1} for the *P* wave velocities is defined and a gradient of 0.0009 s^{-1} for *S* wave velocities, respectively. The velocity models for the 3-D migration represent a 1-D velocity model with an average Moho depth of 50 km.

horizontal interfaces and 1-D velocity structures in these methods, however, may lead to distorted interfaces with incorrect dip and lateral position of lithospheric interfaces dipping ≥10° [*Langston*, 1977; *Cassidy*, 1992; *Yilmaz*, 2001].

More advanced migration methods (e.g., Kirchhoff-style migration [*Levander et al.*, 2013] or the 2-D teleseismic generalized Radon transform migration [e.g., *Miller et al.*, 1987; *Bostock et al.*, 2001; *Rondenay et al.*, 2005]) based on high-frequency, single-scattering wave fields use less a priori assumptions and can reveal high-resolution images of seismic interfaces. Such migration or inversion approaches, however, require a considerably high-quality data set with a suitable dense seismic network configuration to resolve seismic discontinuities at a certain depth level.

In this study, we follow the 2-D migration scheme of *Abe et al.* [2011] for common conversion point (CCP) stacking which includes a high-frequency ray approximation for phase conversions at first-order seismic discontinuities. In this approach Snell's law for *P*-to-*S* phase conversions of teleseismic waves is applied by considering the orientation of the conversion interface predefined by the background velocity model. Deviations in the migrated conversion signal to the predefined geometry of the first-order seismic discontinuity in the velocity model are used to iteratively adopt the geometry of the discontinuity in the 2-D migration velocity model. This iterative approach allows to derive a consistent image of the geometry of first-order seismic discontinuities in relation to *P*-to-*S* phase conversions and the velocity structure. To resolve lateral variations in the seismic structure perpendicular and along array alignments, we extend the method from 2-D to 3-D, including first Fresnel volumes and phase weighting of the linear amplitude stack following the approach of *Frassetto et al.* [2010]. Furthermore, we introduce a quality assessment of imaged conversion features based on the data coverage to identify well-resolved features in the 3-D migration. Dipping interfaces or lateral variations in the velocity structure are revealed by an iterative application of the migration scheme using a trial-and-error approach. Our migration approach is based on the back projection of receiver function amplitudes to grid nodes, which fulfills (1) Snell's law for *P*-to-*S* phase conversions of teleseismic waves considering the orientation of the interface and (2) the first Fresnel volume approximation of the teleseismic wavefield.

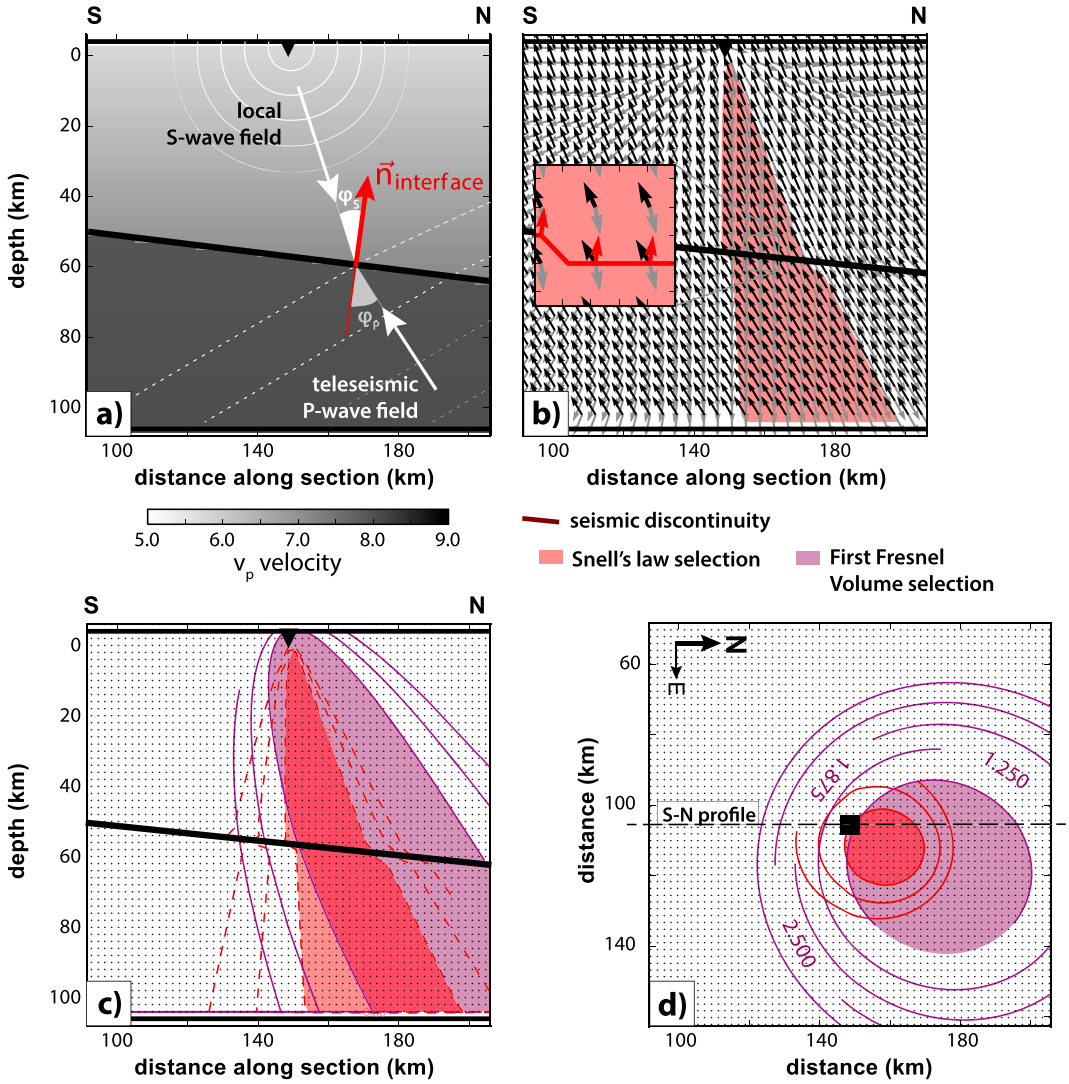

Figure 5. Principle of the 3-D migration approach for *P*-to-*S* receiver function signals used in this study for a dipping conversion interface. (a) Schematic overview of migration grid node selection by Snell's law. (b) Time gradient fields of local downward propagating *S* waves (gray arrows), upward propagating *P* waves from a teleseismic source (black arrows), and surface normal of conversion interface (red arrows in inset). Red volume indicates region, where Snell's law criterion is fulfilled. (c) Areas of fulfilled Snell's law (red) criterion and first Fresnel volume (purple) criterion for the selection of grid nodes to migrate receiver function signals. (d) Lateral extent of migration selection criteria at 50 km depth in map view, Snell's law (red filled area), and first Fresnel volume (purple filled area, numbers of contour lines represent the dominant period of the first Fresnel volume).

To include Snell's law and the first Fresnel volume in the migration, we compute first 3-D traveltimes and associated time gradient fields on a regularly spaced grid using the fast marching method for layered media [*Rawlinson and Sambridge*, 2004; *Kool et al.*, 2006]. The wavefield calculations comprise the forward propagation of teleseismic waves and the backward propagation of the local *P* and *S* wavefields from each receiver through a given 3-D velocity model or a regional 1-D velocity model following the velocity structure of a minimum 1-D *P* and *S* wave model, for example.

The calculation of 3-D wavefields for each station-event pair inherently takes into account moveout corrections. Consequently, the data set of teleseismic events do not have to be limited to a certain back azimuth range to obtain constructive interference from receiver function signals from dipping converters.

First, we define the local lag time field beneath the array for each station (t_{PS}) based on the backward propagated *S* and *P* time fields from each station (Figure 5a). Traveltime fields are calculated on a uniform 3-D grid

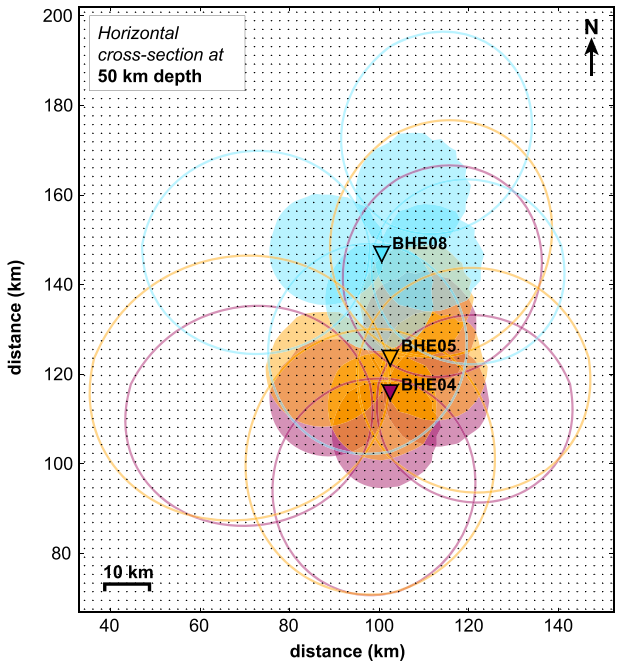

Figure 6. Lateral overlap of migration projection volumes for a 2-D station array at 50 km depth. Filled circles indicate the area of the Snell's law criterion for RF with different back azimuths and distances. Circles with the same color correspond to RF recorded at the same station. Corresponding first Fresnel volumes are shown by larger, empty circles in same colors. Stations are indicated by black contoured triangles.

with 2 km spacing, which limits the resolution of the migration images to 2 km. To define potential *P*-to-*S* conversion nodes in the 3-D grid for each wave field, we use time gradients in each node of the back propagated *S* wave (∇S_{local}) and the forward propagated teleseismic *P* wave ($\nabla P_{\text{teleseismic}}$) field in combination with the surface normal ($\vec{n}_{\text{interface}}$) of the closest underlying interface (Figure 5b). The angle θ has to be π to have a *P*-to-*S* conversion and is defined as following:

$$\frac{(\nabla P_{\text{teleseismic}} + \nabla S_{\text{local}}) \cdot \vec{n}_{\text{interface}}}{|\nabla P_{\text{teleseismic}} + \nabla S_{\text{local}}||\vec{n}_{\text{interface}}|} = \cos(\theta) \tag{1}$$

We allow for small deviations in Snell's law up to 5%, in parallel of $\vec{n}_{\text{interface}}$ and the sum of $\nabla P_{\text{teleseismic}}$ and ∇S_{local}, to consider numerical limitations in accuracy of time gradients, small-scale lateral variation in velocities, and topography along the conversion interfaces. In comparison to the first Fresnel volume, following wave-based principles and the Born approximation to determine constructive contributions to observed signals at a receiver [*Červený and Soares*, 1992; *Husen and Kissling*, 2001] the Snell's law criterion is more restrictive in selecting the migration grid nodes (Figures 5c and 5d). Although the Snell's law area represent mainly a subset of the first Fresnel volume above the conversion interface (see Figures 5c and 6), we use the first Fresnel criterion as an additional criterion to define migration grid nodes. The advantage of smaller projection areas defined by Snell's law is a more adequate stacking of receiver function signals assigned to *Ps* converted phases [*Abe et al.*, 2011]. We use a uniform value of 1.25 s to define the Fresnel volume, which is the dominant wavelet period and corresponds to the upper limit of the band-pass filtering of the teleseismic waves prior to the RF deconvolution. Deviations in dominant periods due to intracrustal conversions with slightly shorter periods have only minor influence on the extent of the first Fresnel volume and are neglected here.

In general, the migration volume has a conic shape, which broadens with depth and is orientated toward the back azimuth of the receiver function (Figures 5c and 5d). Based on the nodes within this migration volume, receiver function amplitudes (rf) are projected along the lag time field using the nearest neighbor algorithm for the selection along the receiver function trace.

4.3.1. Lateral Sensitivity of 3-D Migration Using a 2-D Array

The lateral resolution of the 3-D migration is defined by the migration depth and azimuthal coverage of the receiver function data set. With increasing depth, the migration volumes broaden from around 10 km

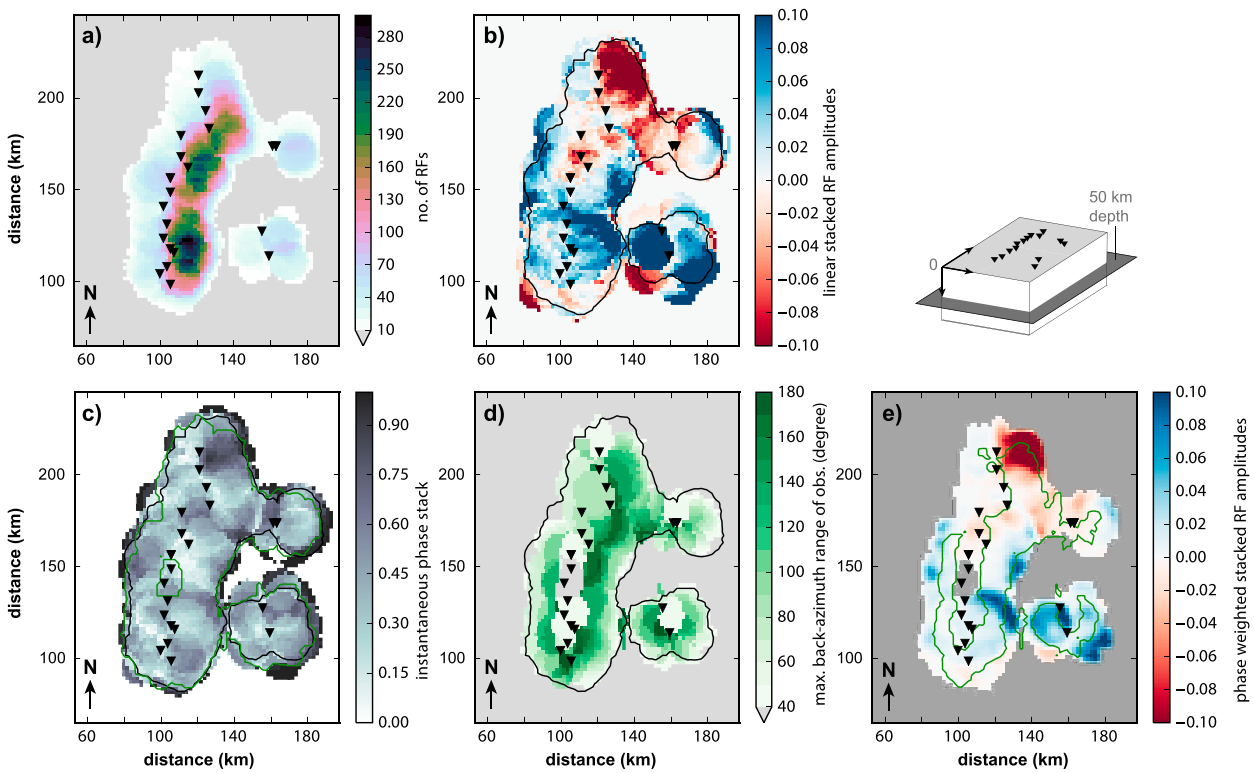

Figure 7. Stacking and weighting scheme of 3-D migrated receiver functions for the western array at 50 km depth. Each station is indicated as a black triangle. Background velocity is a 2-D horizontally layered model based on the minimum 1-D *P* and *S* wave velocity models (Figure 4) with a first-order seismic discontinuity (Moho) at 50 km depth. (a) Lateral distribution of number of traces (receiver function signals) in each bin. (b) Linear amplitude stack, black line outlines region with at least 10 different RF per bin (also in Figures 7c and 7d). (c) Instantaneous phase stack of RF, the green line indicates a minimum range in back azimuth coverage of 40° per bin. (d) Minimum range in back azimuth coverage of stacked RF per bin. (e) Smoothed and phase-weighted amplitude stacks [e.g., *Schimmel and Paulssen*, 1997; *Frassetto et al.*, 2010] of bins with at least 10 receiver functions and a minimum back azimuth difference of 40°. Green line outlines the well-resolved region at this depth with a minimum range in back azimuth coverage of 90°. See text, section 4.3.2, for more details on the stacking.

diameter in the upper and middle crust to a diameter of 20 km at the crust-mantle boundary (at 50 km depth, Figures 5b–5d). At greater depths, receiver function amplitudes are therefore projected on larger areas and the interference of *Ps* phase signals from neighboring stations are more likely than in the shallower crust (Figure 6). In the upper crust at 0–10 km depth, overlapping of migration volumes is more limited in space and seismic structures can only be resolved directly beneath the 2-D array. This requires, however, teleseismic events in line with the array from both directions. Assuming an optimal data coverage of receiver functions, lateral variations in the Moho depth beneath the Himalayan orogenic wedge (at 50 km depth) within 40 km east and west of each array could be resolved. At middle crustal level (around 20 km depth) lateral variations would be only resolved within 20 km distance to the array.

Limitations in the back azimuth range of our data set will significantly reduce the lateral resolution of the 3-D migration. With a poor data coverage of teleseismic events from the south or the north azimuth, as it is the case for the western and eastern GANSSER arrays (Figure 2), structures directly beneath the south-north oriented 2-D array are only poorly resolved. This is in particular true below middle crustal levels (from around 20 km depth), where deflection of migration volumes toward the back azimuth direction becomes significant. For such a distribution of teleseismic events and our array configuration, the areas resolved by 3-D migration reveal a "cone-like" shape with depth to both sides of the 2-D array (Figure 6). With increasing depth, the sensitivity of the migrated and stacked receiver function signals is laterally shifted away from the station array (Figures 7a and 7d).

4.3.2. Linear Common Conversion Point Stacking of Amplitudes With Phase Weighting

By linearly stacking individually migrated receiver function signals, following the principle of common conversion point (CCP) stacking [*Dueker and Sheehan*, 1997], laterally coherent conversion structures can be imaged with a sufficiently homogeneous data coverage. For a strongly heterogenous distribution, like it is the case for both GANSSER arrays, we consider only bins (nodes) with at least 10 RF traces for stacking (Figure 7a).

In tectonically complex regions linearly stacked amplitudes of conversion structures can be still distorted by scattering, reverberation, or diffraction signals generated at dipping structures, shear zones, or sedimentary basins [*Frassetto et al.*, 2010]. To reduce the effect of these signals in the migration and to enhance intrinsic *Ps* phase signals of conversion structures [*Frassetto et al.*, 2010], we add a phase weighting, which involves the mean instantaneous phase stack (w_{phase}) in each bin (Figure 7c). The instantaneous phase $\phi_{s,e}(x,y,z)$ is obtained from the analytic RF signal for each event-receiver pair. The phase stack (w_{phase}) is therefore defined as follows:

$$w_{\text{phase}(x,y,z)} = \frac{1}{N}\left|\sum_{s=1}^{\text{station}}\sum_{e=1}^{\text{event}} e^{i\phi_{s,e}(x,y,z)}\right| \tag{2}$$

Multiplied with the mean instantaneous phase stack the normalized linear amplitude stack of RF signals ($rf_{e,s}(t_{PS})$) defines then the RF signal in each bin (m):

$$m = w_{\text{phase}}\frac{1}{N}\sum_{s=1}^{\text{station}}\sum_{e=1}^{\text{event}} rf_{e,s}(t_{PS}) \tag{3}$$

4.3.3. Determination of Well-Resolved Regions in 3-D Migration Image

Applied to the 3-D migration, phase weighting performs well in areas that are well sampled by different receiver function signals with variable epicentral distance and from a large range of back azimuths. To avoid that stacked signals with nearly identical back azimuths and distance outside well-resolved areas dominate the RF structure, we compute the minimum range in back azimuth coverage in each bin to evaluate the quality of the stacked and phase-weighted receiver function signals (Figure 7d). For the 3-D migration of the two GANSSER arrays, we define a minimum range in back azimuth coverage of 40° to define regions with at least fair resolution. This relatively low threshold accounts for the limited data coverage in teleseismic events for both arrays (Figure 2) and allows to image structures in the orogenic wedge at lower, middle, and upper crustal levels in addition to the crust-mantle boundary. A higher and more adequate threshold of 90° is used to highlight well-resolved areas in the 3-D migration image used for interpretation.

Finally, to reduce effects of high-amplitude anomalies in single migration bins, we apply lateral smoothing over three grid nodes, which is equivalent to 6 km.

4.4. A Priori Lithospheric Velocity Model of Bhutan for 3-D Migration

For the migration of RF along the two GANSSER arrays in Bhutan, we use independently derived crustal velocities defined from a local minimum 1-D model (Figure 4 and section 4.2). To image the lithospheric structure across Bhutan, we initially focus on the accurate imaging of the Moho geometry and, therefore, approximate the minimum 1-D velocity model to a two-layer model with a crustal and an upper mantle layer. In both layers, velocities (v_p and v_s) increase uniformly with depth following the velocity structure of the minimum 1-D model (Figure 4).

We use these velocity gradients in combination with varying Moho geometries to define the 3-D *P* and *S* wave velocity model for the receiver function migration. As an initial velocity model for the 3-D migration, we use a flat horizontal Moho interface at 50 km depth, based on our preliminary results from the single-station time-to-depth migration (section 4.2 and Figure S3 in the supporting information).

4.5. Sensitivity of 3-D Migration to Velocity Structure

The iterative application of the 3-D migration scheme with its sensitivity to the geometry of first-order isotropic velocity discontinuities in the migration velocity structure, allows the assessment of the geometry of imaged conversion structures in relation to the background velocity model. Besides its influence on the depth of *Ps* phase arrivals, the background velocity model affects the shape, width, and direction of migration volumes by considering the orientation of isotropic velocity discontinuities (Figure 5). The application of a true 3-D migration scheme in combination with a 2.5-D background velocity model allows to explore the model space for Moho geometries that show a high consistency with the imaged and weighted conversion structure.

4.6. Potential Artifacts in Migrated Image

Migration artifacts may result from poor data coverage, incorrect velocity models, too large projection volumes or from conversion multiples using the continuous RF signal in the migration procedure. Even by the application of strict migration criteria and the quality assessment, multiples may remain if projected into

well-resolved areas and if they yield a coherent signal. Especially, multiples from shallow intracrustal converters can coincide with positive polarity *Ps* Moho phases. Upper to middle crustal conversion structures at 15–20 km depth can generate positive polarity *PpPs* phases with delay times similar to *Ps* phases originating from the crust-mantle boundary at 50–60 km depth. Consequently, a careful evaluation of the Moho depth and geometry imaged by the 3-D migration needs to account for potential intracrustal multiples.

4.7. Resolution Assessment for 3-D Migrated Moho and Intracrustal Structures

The resolution of lithospheric converters imaged by 3-D migration depends on the wavelength of the converted wave, conversion depth, seismic velocities, and the type of conversion interface. We distinguish between different types of converters: (1) first-order isotropic velocity discontinuities and (2) intracrustal shear or fault zones with contrast in isotropic shear velocity or contrast in anisotropy in *P* wave velocity.

The most prominent isotropic velocity contrast is the Moho as discontinuity between the petrological differentiated lower crust and the upper mantle. In our 3-D migration the Moho can appear less pronounced compared to shallower intracrustal converters due to the applied phase weighting [*Frassetto et al.*, 2010] (Figure 9). With increasing depth, migration volumes become larger (Figure 5b) and the variability in phase arrivals increases. Therefore, the overall coherency in the stacked instantaneous phase signals decreases and variations in the amplitude of converters in the 3-D migration independent of the strength of the velocity contrast are likely.

To remove small-amplitude signals in the phase-weighted migration without sufficient relevance, we consider only signals with amplitude larger than 1% of the average phase-weighted stacked receiver function signals. In the presence of anisotropic structures or low- or high-velocity layers in the upper or middle crust the conversion signal of the Moho can be distorted and imaged with low resolution and intensity [*Sherrington et al.*, 2004].

The vertical resolution of RF is defined by approximately half the wavelength of converted phases and the velocity of the converted wave above the discontinuity [*Bostock and Rondenay*, 1999; *Rychert et al.*, 2007]. For the GANSSER receiver function data set, we obtain an average wavelength of 2.5–3 s for Moho *Ps* arrivals. This corresponds to a vertical resolution of 5–6 km for a high-quality receiver function, comparable to results of *Spada et al.* [2013]. Locally, we obtain such resolution of the Moho in the 3-D migration by using only one station, while in the combined 3-D migration of different stations the Moho signal generally broadens and becomes less pronounced (Figures 9 and 12). Irregular small-scale topography along the Moho [*Clouser and Langston*, 1995; *Spada et al.*, 2013], attenuation and modification of converted Moho signals due to complex intracrustal converters [*Spada et al.*, 2013] or a highly nonuniform distribution in back azimuth of stacked signals can cause broadening and a lower resolution of the Moho, especially in the stacking of individual vertical cross sections of the migration image (e.g., shown in Figure 10 in comparison to Figure 9).

In contrast to the Moho, we associate intracrustal converters with tectonic interfaces of several kilometer thickness, with either an anisotropic fabric or contrast in shear wave velocity. The sensitivity of RF to such velocity contrasts has been shown in various studies [e.g., *Levin and Park*, 1998; *Sherrington et al.*, 2004; *Bianchi et al.*, 2010; *Schulte-Pelkum and Mahan*, 2014a]. Along the two GANSSER arrays, conversion signals prior to the Moho phase reveal complex back azimuth-dependent pattern of amplitudes and delay times (e.g., Figure 3). These patterns are also present in the transverse RF signal (e.g., Figure S4 in the supporting information), however, less complete in back azimuth coverage than for the radial component due to lower signal-to-noise ratios in the transverse raw seismic signal. The appearance of back azimuth-dependent receiver function signatures on radial and transverse components are characteristics for seismic structures with either dipping isotropic velocity contrasts, dipping shear zones with anisotropy or horizontal zones with plunging axis anisotropy [*Schulte-Pelkum and Mahan*, 2014a]. An assessment of the strength and orientation of the anisotropic zone requires a complete back azimuth coverage of transverse and radial components [e.g., *Cassidy*, 1992; *Levin and Park*, 1997, 1998]. However, for most of the stations of the GANSSER network the combined back azimuth coverage is incomplete and therefore limits the interpretation of intracrustal converters. The appearance of intracrustal converters either interpreted as isotropic velocity impedance contrasts or shear zones was shown by previous studies in the Himalaya, with interpretations mainly focusing on the upper to middle crustal detachment zone of the Main Himalayan Thrust [e.g., *Schulte-Pelkum et al.*, 2005; *Singh et al.*, 2010; *Caldwell et al.*, 2013].

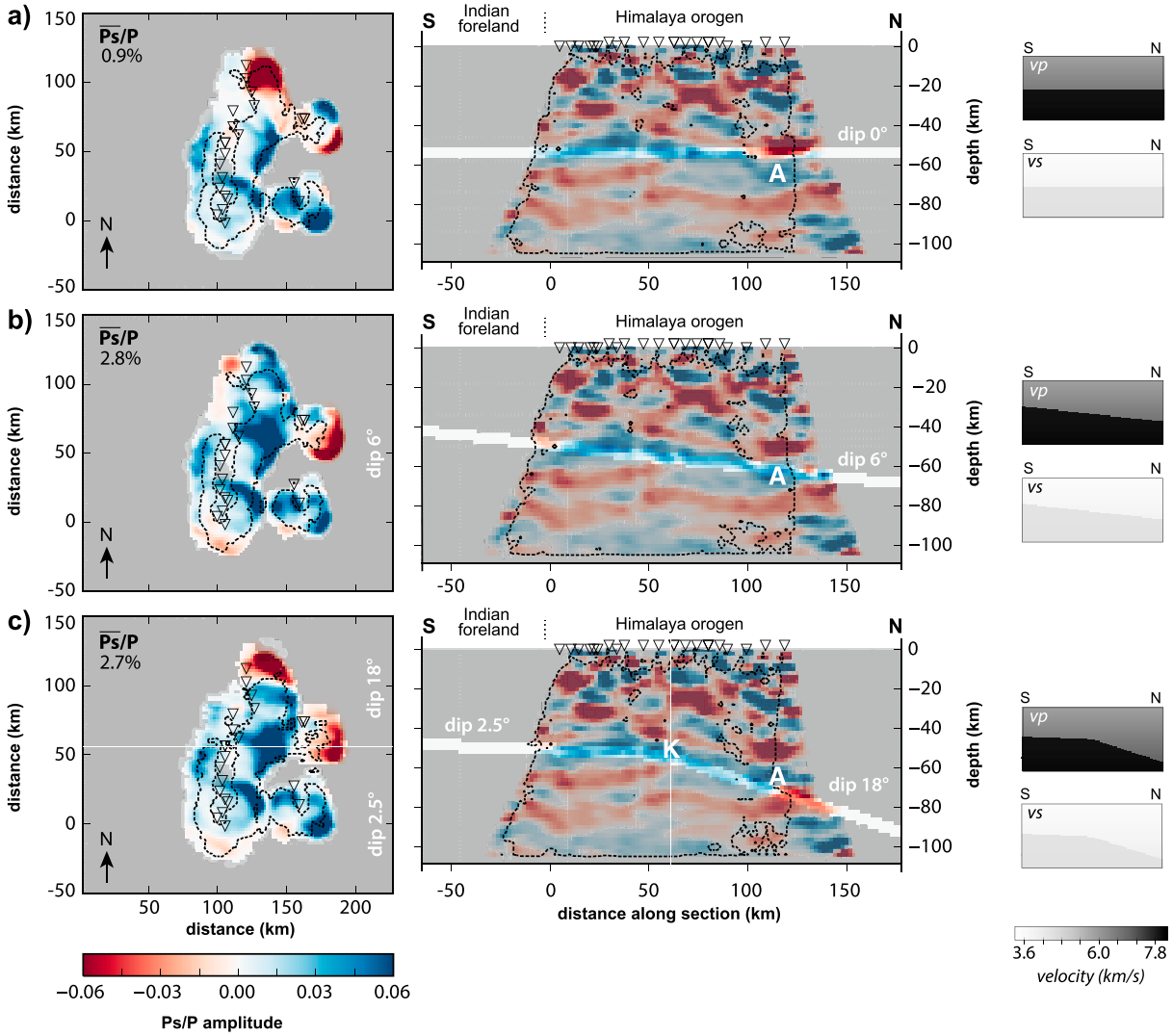

Figure 8. Dependency of migration background velocity model and geometry shown for the western GANSSER array. (left column) Phase-weighted, stacked, and migrated radial RF amplitudes within 3 km depth (±1 grid node) of the first-order velocity discontinuity of (a–c) different input models. Grey area corresponds to areas with less than 10 different observations and a minimum back azimuth range of less than 40°. Black dotted line outlines well-resolved area with a minimum back azimuth range of 90°. Images are laterally smoothed over 6 km. (middle column) Two-dimensional south-north stacks of migration with different velocity models. White areas highlight depth sections shown on the left (minimum back azimuth range of 40°, at least 10 teleseismic rays). (right column) *P* and *S* wave velocity models used in the migration shown in Figure 8 (left and middle columns). A indicates area with a downdipping Moho signal. K indicates the location of a kink in the imaged Moho signal.

For upper crustal shear zones we obtain a maximum vertical resolution of 3 km considering a shorter RF signal wavelength of 1.8 s (Figure 3). The minimum vertical resolution of around 3 km also represents the minimum shear zone width, which can be resolved by the 3-D migration. In western and eastern Bhutan, however, we image intracrustal converters with a vertical resolution of 3–8 km (Figures 8 and 12). Similar to the vertical resolution of the Moho, we explain this lower resolution of imaged intracrustal structures by small-scale lateral irregularities in the anisotropy pattern in addition to less continuous and uniform deformation zones across and perpendicular to the orogenic wedge in Bhutan.

5. Results

5.1. Lithospheric Structure Beneath Western Bhutan

For the migration in western Bhutan, we first tested velocity models with different Moho geometries by applying our 3-D migration method iteratively (as described in section 4.3). The primary focus in this iterative application is the accurate imaging of the main lithospheric structure and secondarily on intracrustal features.

We begin the 3-D migration with a horizontally layered velocity model (1-D model) and a Moho at 50 km depth following the results of section 4.2 on the Moho depth constrained by a modified H-κ approach. The migrated receiver functions confirm a Moho depth of around 50 km depth in the south (Figure 8a) with a clear indication for a dipping Moho north of 27.4°N (A in Figure 8). We adjust the velocity model and use a Moho geometry with a constant northward dip of 6° (Figure 8b) and another model with a kink in the northward dip (Figure 8c) as indicated in the initial migration. The migrated Moho converters correlate well with the crust-mantle discontinuity predefined by the velocity model (Figure 8b), reaching an average lateral RF amplitude relative to the direct *P* phase arrival (*Ps*/*P*) within the Moho transition zone of 2.8% for the uniformly dipping 6° model and 2.7% for the nonuniformly dipping model. These values of the average lateral RF amplitude are 3 times higher than for the flat Moho model. Although the migration with the uniformly dipping velocity model reveal a slightly higher (+0.1%) average amplitude along the velocity discontinuity, the nonuniformly dipping Moho model covers better the abrupt steepening of the imaged Moho toward the north and the shallow dipping of the Moho in the southern part of the orogenic wedge (Figure 8c). Therefore, we prefer the nonuniformly dipping velocity model in the migration to image most accurately the Moho geometry of the underthrusting Indian crust in western Bhutan. Additional evidence for this steepening of the Moho toward the north is provided by a well-constrained lower crustal earthquake at 76 km depth (more details about this can be found later in this section).

The abrupt steepening of the Moho to a dip of around 18° is imaged at around 27.3°N, ~60 km north of the MFT, and at 48 ± 5 km depth (K in Figure 8c). The location of this Moho kink is well resolved east of the array at around 89.8°E (profile WEST 3 in Figure 9). South of the kink, the Moho of the underthrusting Indian lithosphere appears to dip at a shallow angle (<3°). Beneath the Lesser Himalaya, at the southern edge of the Himalaya, Moho conversions appear to be less clear and might be distorted by multiples of intracrustal converters (profile WEST 1 to WEST 3, Figure 9 and section 4.7). An extrapolation of the Moho converter imaged in profile WEST 3 in Figure 9 toward the southern Himalaya front suggests a crustal thickness of the Indian lithosphere of approximately 46 ± 5 km before entering the orogenic collision in western Bhutan.

Besides the Moho, several intracrustal structures with positive and negative RF amplitude polarity are imaged in western Bhutan. These intracrustal structures appear less homogeneous and continuous in the migrated images as the Moho. This can be explained by smaller migration volumes at shallower depth (Figure S6 in the supporting information) and stronger lateral variations in the lithospheric structure at middle and upper crustal depths. One of the most pronounced intracrustal converter is a ramp-like structure at middle crustal depth beneath the northern Greater Himalaya with a positive phase arrival amplitude (Rw in profile WEST 3, Figure 9). Beginning at around 27.63°N, we can resolve a 18 ± 2° northward dipping structure over a distance of 30 km. After a gap of about 10 km width it continues with reverse polarity toward the Lesser Himalaya in the south as a nearly flat structure (profile WEST 1 and WEST 2, Figure 9). The limitation in data coverage at shallow depth and station spacing prohibits a clear imaging of a frontal ramp breaching of this 12 km deep converter to the surface at the southern Himalayan front in association with a shallow frontal ramp of the Main Himalayan thrust. Only a weak continuous signal with positive polarity appears (fRw in profile WEST 1 and WEST 2, Figure 9), which could indicate a steep frontal ramp to the MCT contact at the surface.

We identify this upper to middle crustal structure as MHT in western Bhutan with an almost subhorizontal part in the south at around 14 km depth and a middle crustal ramp (dipping 18° north) beneath the Higher Himalaya. In comparison to other parts of the Himalaya, this positive RF signal of the MHT in the southern part is comparable to RF results of *Schulte-Pelkum et al.* [2005] in eastern Nepal. Instead of an isotropic velocity contrast, these RF signals of the MHT in eastern Nepal are interpreted as an anisotropic shear zone representing the upper crustal detachment zone. This anisotropic shear zone appears to change its seismic characteristics beneath the Higher Himalaya, where we image the MHT as negative RF arrival and ramp structure (discussed in more detail in section 6.2).

Similar to the geometry of the Moho, this intracrustal structure shows an abrupt steepening in the north, represented by the positive and negative ramp amplitude structures. The kink (K_{MHT} in profile WEST 2, Figure 9), however, does not coincide with the kink in the Moho and is located around 25 km farther north at 27.5°N.

Wide-angle reflections in the middle crust at around 27.75°N along the two INDEPTH (International Deep Profiling of Tibet and the Himalaya) profiles Tib-1 and Tib-3 [e.g., *Alsdorf et al.*, 1998a, 1998b; *Hauck et al.*, 1998] (locations of Tib-1 and Tib-3 are shown in Figure 1) coincide with the ramp structure imaged by receiver functions in the north (Figure 10). Furthermore, the dipping Moho imaged by receiver functions

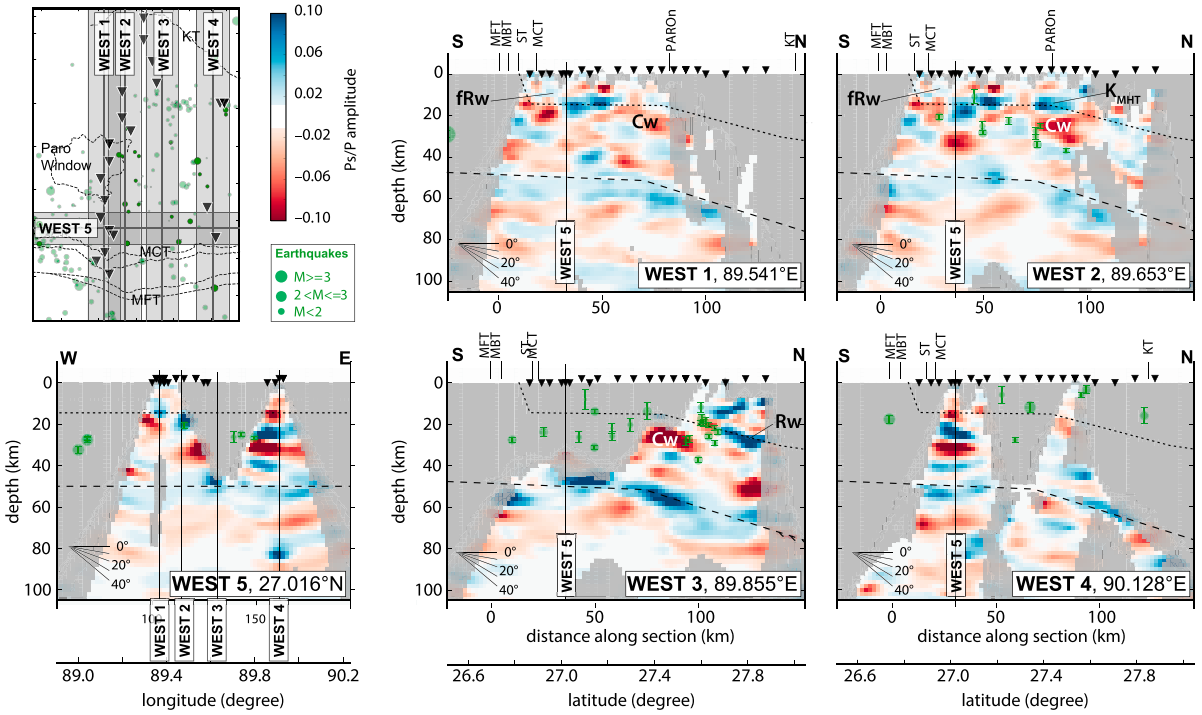

Figure 9. Individual cross sections through the 3-D migration image in western Bhutan; radial RF are linearly stacked, including phase weighting. Each cross sections is laterally averaged over ±2 neighboring grid nodes; only nodes are considered, which have at least 10 observations in total and have an absolute amplitude of the conversion signal of at least 1% of the direct *P* arrival. Regions without a sufficient resolution, back azimuth coverage <40°, and in total <10 RF are marked in gray. Black dashed line indicates the Moho of the velocity model used in migration. Green circles represent hypocenter location of well-locatable (GAP<200° and observations ≥10) earthquakes recorded by the GANSSER network in the regions of the individual cross sections. Seismic stations are shown as black triangles. The geometry of the MHT defined by *Coutand et al.* [2014] with thermokinematic models in western Bhutan is indicated in each cross section with a fine dotted line. fRw (frontal ramp west), K_{MHT} (kink of MHT geometry), Cw (intracrustal converter pattern), and Rw (middle crustal ramp of MHT) point out areas with distinct intracrustal converters described in the text.

(profile WEST 4 in Figure 9) at ~90.1°E is consistent with Moho reflections at around 70 km depth along profile Tib-1, located around 80 km to the west of our observation (Figure 10). Although the stacked south-north cross section in Figure 10 of the individual profiles in Figure 9 reveal a negative conversion signal in the region of the reflection data, we argue that the clear trend of a downdipping Moho in the profiles WEST 1 to WEST 4 coincide in a first-order approximation with the Moho results of the INDEPTH reflection data. The application of a similar average crustal *P* wave velocity (approximately 6 km/s) for the migration of the reflection profiles and our receiver functions precludes an apparent coincidence of these structures due to differences in migration velocities. The occurrence of a lower crustal earthquake at 76±1.3 km depth (6 June 2013) in northwestern Bhutan (Figure 10) confirms the steepening subduction of the Indian lithosphere toward the north and its extent from the Yadong-Gulu graben toward central Bhutan. This earthquake is well constrained in its hypocenter (90.255°E/28.0158°N) using the GANSSER network including the IRIS station (LSA) in Lhasa and shows clear *Pg* and *Pn* phases in record sections as evidence for its crustal location.

At middle to lower crustal depths, additional high-amplitude negative converters occur with a general northward dipping geometry (Figure 9). North of the Moho kink at around 27.5°N, a continuous converter of 20 km length with negative polarity is imaged between 20 and 30 km depth (Cw in profile WEST 1 to WEST 3 in Figure 9). Due to its length, amplitude, and along-strike consistency, we interpret this RF signal as a strong indication for a significant and abrupt change either in seismic velocity or in anisotropy related to an extensive shear zone (see section 4.7). Characteristics of such an intracrustal seismic structure in the RF signal are shown in the radial RF signal of station BHW13 with a continuous change in delay times of a dominant, negative middle crustal conversion with back azimuth (Figure S5 in the supporting information). Its latitude and depth of this converter coincides with a zone of strong seismic anisotropy in the neighboring region of the Sikkim Himalaya, represented as negative amplitude signal and as anisotropic signature on transverse receiver functions [*Singh et al.*, 2010].

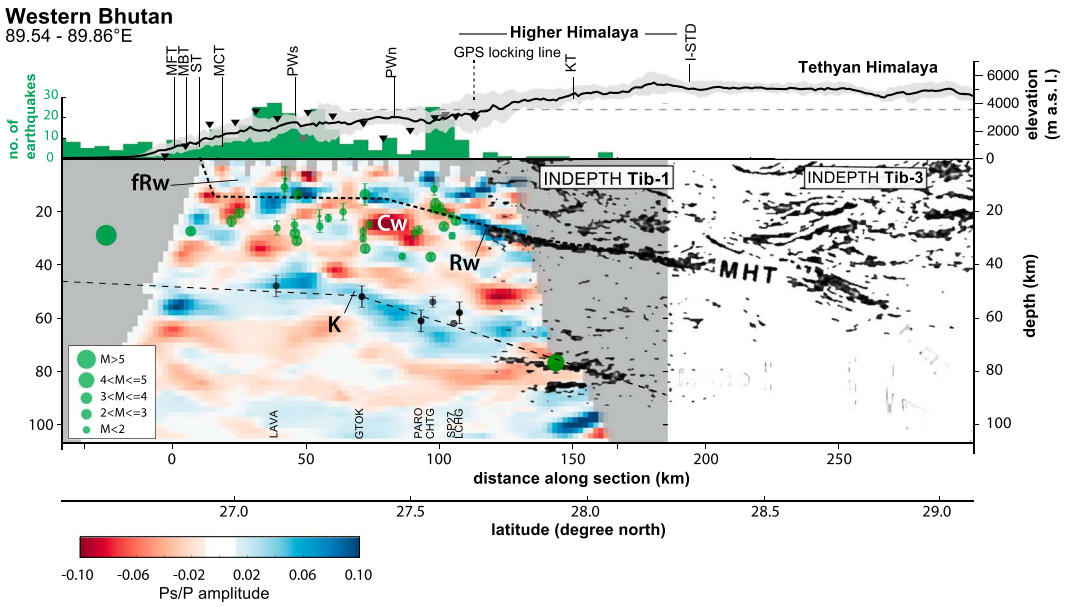

Figure 10. Two-dimensional stack of individual cross sections through 3-D migration image of radial receiver functions, linearly stacked with phase weighting in western Bhutan. Cross section is composed of profile WEST 1 to WEST 3 from Figure 9. Each cross section is laterally averaged over ±2 neighboring grid nodes, only those nodes are considered, which have at least 10 different RF signals in total and have an absolute amplitude of the conversion signal of at least 1% of the direct *P* arrival. The geometry of the MHT defined by *Coutand et al.* [2014] in western Bhutan is indicated by fine dotted line. The seismic reflection profiles INDEPTH Tib-1 and Tib-3 from *Hauck et al.* [1998] are shown in the background. Hypocenter location of well-locatable (GAP<200° and observations ≥10) earthquakes recorded by the GANSSER network are marked by green circles. Black circles indicate the Moho depth of *Acton et al.* [2011], with RF uncertainties in depth indicated by error bars in Sikkim (names of the corresponding stations are shown at the bottom of the profile). Mean topographic profile for this cross section is represented by the bold black line and standard deviation by the shaded gray area. K (kink in Moho geometry), Cw (intracrustal converter), fRw (frontal ramp of MHT), and Rw (middle crustal ramp of MHT) point out areas with distinct intracrustal converters described in the text.

5.2. Lithospheric Structure Beneath Eastern Bhutan

The migration of phase conversion signals in eastern Bhutan with a uniform, horizontal background velocity model with a Moho at 50 km depth reaches an average relative conversion signal amplitude (*Ps*/*P*) of 2.2% (Figure 11) for fairly well resolved regions at this depth. This amplitude value is similar to the value obtained with the final kinked Moho velocity model of 2.7% for western Bhutan (Figure 8). For comparison, the initial migration with exactly the same background velocity model with a horizontal Moho in western Bhutan reaches only 0.9%.

Positive Moho conversion signals are migrated to almost similar depth across the migration volume and image a continuous Moho structure from the southern Himalayan front to 27.8°N (profile EAST 2 and EAST 3 in Figure 12). The high-amplitude conversion in profile EAST 1 (Figure 12), above the 50 km depth line is mainly caused by the migration of RF from a single station without a stacking of RF from neighboring stations. As shown in Figure 11, the back azimuth range of this migrated high-amplitude conversion is lower than 90° and outside the well-resolved area NW of station BHN08. Furthermore, multiples from an intracrustal converter, like the positive RF signal at ~20 km (profile EAST 1 in Figure 12), have larger delay times and do not lead to constructive interference with *P*-to-*S* RF signals from the Moho at this depth.

Deeper positive conversion signals appear only at the northeastern edge of the fairly well resolved migration volume at around 62 km depth (M? in profile EAST 3 and EAST 4 in Figure 12), but additionally to positive conversion structures at 50 km depth with a similar amplitude. This deeper converter, imaged with a data coverage of less than 110° back azimuthal coverage, can be either explained as a northward dipping Moho east of our profile (Arunachal Pradesh) or as a migration artifact associated with intracrustal multiples (see section 4.1) from a converter imaged at around 20 km depth (profile EAST 4 in Figure 12). Based on the clearly imaged horizontal Moho signal in the remaining eastern region at the same latitude (profile EAST 4 in Figure 12),

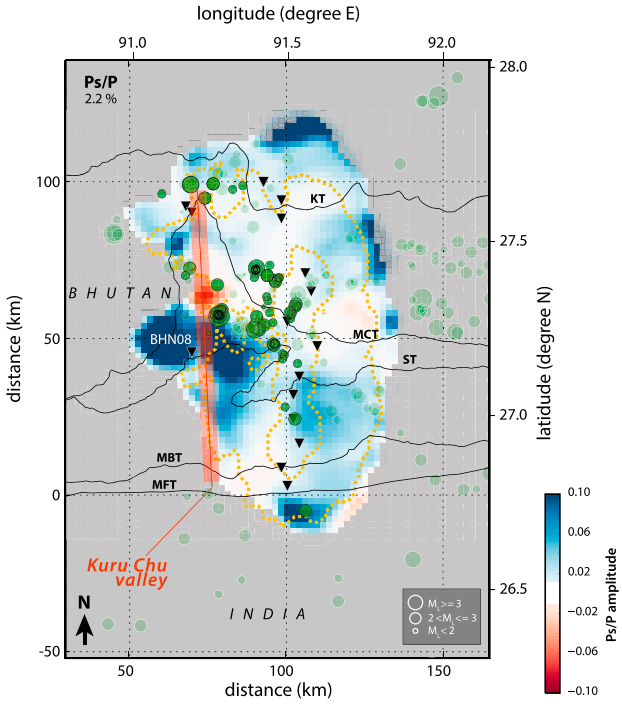

Figure 11. Horizontal cross section at 50 km depth through 3-D migration image of radial receiver functions, linearly stacked with phase weighting along the eastern GANSSER array in Bhutan, similar to Figure 8. Stations of the eastern array, used for the migration, are indicated by black triangles. Green circles represent earthquakes recorded by the GANSSER network. Well-resolved regions by the 3-D migration with ≥10 receiver functions and minimum back azimuth coverage range in stacked RF of 90° at 50 km depth is outlined by orange dotted line.

however, we do not consider this local conversion as a relevant structure for the main lithospheric structure in eastern Bhutan and interpret it as possible migration artifact.

Although the imaged Moho converter suggests a mainly constant crustal thickness for eastern Bhutan south of 27.8°N, apparent deviations of few kilometers are present. Strong, positive conversion signals at 47 ± 4 km depth indicate a shallower Moho toward the south within 70 km distance to the MFT beneath the Kuru Chu valley (profile EAST 1 in Figure 12). In the eastern part of eastern Bhutan, we can continuously trace this Moho depth of 47±4 km depth toward the southern Himalaya front (profile EAST 3 in Figure 12). Along the embayment of the MCT where this tectonic structure is locally displaced at the surface by around 50 km to the north [*Long et al.*, 2011a], however, limited data coverage of teleseismic events from south and west and the lack of stations in the vicinity of the Indian foreland precludes an imaging of the Moho in this region (profile EAST 1 in Figure 12).

For the intracrustal converters, the 3-D migration indicates strong lateral variations along the strike of the Himalayan orogenic wedge (Figure 12). Listric structures are imaged, which reach from the upper crust beneath the Lesser Himalaya down to middle crustal depths beneath the Greater Himalaya Sequence at 27.3°N (Ce in profiles EAST 2 and EAST 3 in Figure 12) in the surrounding of the Kuru Chu Valley. These structures are characterized by subparallel bands of positive and negative polarity, as shown in the profile EAST 2 in Figure 12. At 91.48°E, the most shallow structure of this pattern at about 12 km depth shows an almost horizontal converter with negative polarity over 20 km length. Only 40 km east of the embayment of the MCT, this pattern of intracrustal converters appears to change. Positive signals are less pronounced or are even missing as shown in profile EAST 3 (Figure 12) at 15–30 km depth. We interpret these patterns of alternating RF signals with depth as potential shear or faults zones of several kilometer thickness (see section 4.7), causing pairs of signals with reverse polarity at the top and bottom of these zones. Consequently, individual signals in this intracrustal conversion pattern do not represent individual shear zones of several kilometer width but rather only 2–3 large-scale intracrustal structures in between these converters with an anisotropic fabric or shear wave velocity anomaly.

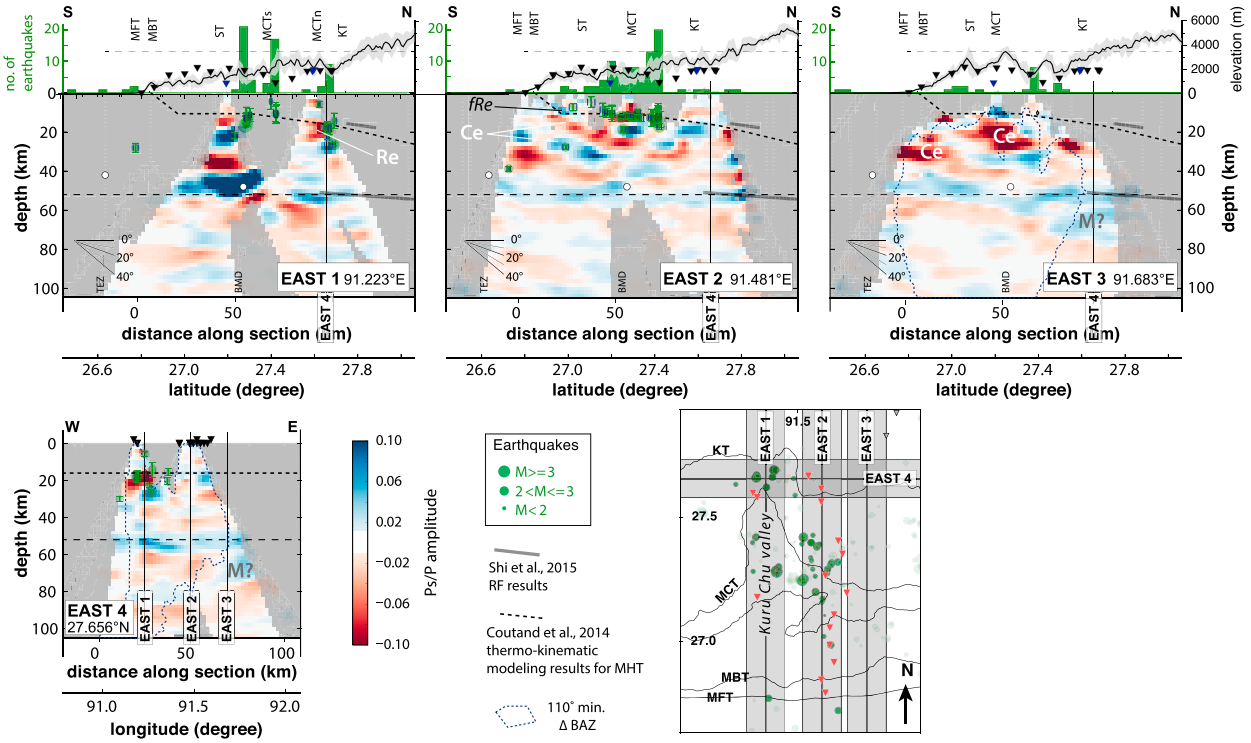

Figure 12. Individual cross sections through the 3-D migration image in eastern Bhutan; see Figure 9 caption for details. White circles indicate the Moho depth derived by *Mitra et al.* [2004] with RF using the H-κ approach for single-station processing; names of the corresponding stations are shown at the bottom of each figure. Receiver function results of the Moho depth and the MHT, based on a 2-D CCP migration, beneath the Tibetan Plateau from *Shi et al.* [2015] at around 92°E are shown as gray lines in profile EAST 1 to EAST 3. The geometry of the MHT defined by *Coutand et al.* [2014] from thermokinematic modeling in eastern Bhutan is indicated in each cross section with a fine dotted line. Mean topographic profile for each profile is represented by the bold black line and standard deviation by the shaded gray area. Re (possible indication of a middle crustal ramp), fRe (frontal ramp of MHT), Ce (intracrustal converter pattern), and M? (apparent deeper Moho signal) point out areas with distinct converters described in the text.

Alternatively, these signals could be interpreted as reverberations from a sedimentary layer of few kilometer thickness on top of the basement and therefore represent artifacts. However, the continuation of these conversion signals over at least eight stations located north of the Siwalik sediment group [*Long et al.*, 2011a, and references therein] are more consistent with thick intracrustal shear or fault zones. In addition, consistent and clear observations of sedimentary signals on phases in receiver functions at stations along the eastern array are missing.

At 50–80 km distance to the MFT, the uppermost negative converter feature of the listric-shaped structures at around 12 km depth coincides with a cluster of well-locatable seismicity recorded by the GANSSER network (profile EAST 2 in Figure 12). Toward the south, the alignment of upper crustal seismicity almost disappears which coincides with the northern edge of the duplex structure of the upper Lesser Himalaya and the associated Sumar-Ramgarh Thrust (ST) [*Long et al.*, 2011a]. Based on these observations, we suggest that the pronounced negative conversion structure imaged at around 12 km depth represents the MHT in eastern Bhutan. Extrapolating this flat MHT structure toward the southern front a positive, steeply rising conversion structure could indicate a frontal ramp (fRe in profile EAST 2 in Figure 12) rooting at the MHT and reaching the surface of the Siwalik fold-thrust belt at an angle of ~40°.

Additional isolated converters with strong amplitudes are imaged by the 3-D migration along the eastern profile. A structure with negative polarity is imaged in the north beneath the Kuru Chu valley at around 27.65°N at 20 ± 4 km depth (Re in profile EAST 1 in Figure 12). This structure is only imaged locally due to the poor data coverage in the surrounding areas but coincides with a cluster of middle crustal seismicity. The converter could indicate an middle crustal intracrustal ramp structure either connected to the MHT or an independent tectonic feature (Re, profile EAST 1 in Figure 12).

6. Discussion

6.1. Along-Strike Variation in the Underthrusting Indian Lithosphere Beneath the Eastern Himalaya

In the Eastern Himalaya in Bhutan, we image significant structural variations in the underthrusting Indian lithosphere along the west-east strike of the Himalaya orogen in this region. These variations occur within 90 km distance between eastern and western Bhutan and indicate important lateral variations in the dynamics of the continent-continent collision in the Eastern Himalaya. We exclude geometric effects causing these variations due to changes in the strike of the Himalayan collision zone. Along the Bhutan Himalaya the orogenic strike is almost uniform and oriented in E-W direction as indicated by the MFT (Figure 1). The Indian lithosphere enters the Himalaya collision zone from the south with a more or less uniform crustal thickness of 46 $\pm$ 5 km and 47 $\pm$ 4 km in western and eastern Bhutan, respectively. These observations (Figures 9, 10 and 12) are consistent with a 44–48 km thick crust beneath the Himalaya foothills in Sikkim derived by RF studies [*Acton et al.*, 2011]. A clear northward dipping Moho beneath the Greater Himalaya, however, is only imaged in western Bhutan. We correlate this first-order regional variation of the Himalaya crustal root with large-scale variations of the Indian lithosphere slab, which subducts beneath Southern Tibet [*Li et al.*, 2008]. According to tomographic images of the present-day upper mantle structure beneath the Tibetan Plateau by *Li et al.* [2008], *Acton et al.* [2010], and *Liang et al.* [2011], subhorizontal underthrusting or subduction of the Indian mantle lithosphere beneath the southern Tibetan Plateau reaches in general only depths of about 250 km.

A notable exception in this upper mantle structure forms a high-velocity anomaly reaching down to 300–500 km depth north of eastern Nepal, Sikkim, and western Bhutan beneath the Tibetan Plateau (90°E, 31°N). This high-velocity anomaly is interpreted as a mantle lithosphere slab and appears to be attached to the underthrusting Indian lithosphere [*Kosarev*, 1999; *Li et al.*, 2008; *Zhao*, 2011] building an approximately 500 km long slab with a relatively narrow width of approximately 300 km and a relatively sharp edge in the east in comparison to its western part (Figure 13). A regional traveltime tomography by *Hung et al.* [2011] with improved resolution using a multiscale, finite-frequency approach is in agreement with such an Indian mantle-slab anomaly.

According to these tomographic results, the region of western Bhutan would be the easternmost part of the Himalaya influenced by the load exerted by this mantle-slab on the Indian lithosphere. Instead of a subduction toward the north, the slab appears to subduct in NNE direction as indicated by the 200 km depth contour line for the top of Indian mantle lithosphere in Figure 13. In its western part the subducting slab reaches this 200 km depth contour north of the Indus-Yarlung suture (IYS) at around 60 km distance, whereas north of western Bhutan the Indian mantle lithosphere crosses this depth range already 90 km south of the IYS (Figure 13). Consequently, a steeper dip of the underthrusting Indian lithosphere into the mantle north of western Bhutan is expected in comparison to the region north of eastern Nepal and Sikkim (light green dashed line in Figure 13 and indicated in the schematic cross section WW'). This correlates well with our observations of a pronounced dip of the Indian Moho beneath western Bhutan from around 50 km depth beneath the southern parts of Bhutan down to around 75 km depth beneath the Higher Himalaya (Figure 13). Farther to the west, in Sikkim and eastern Nepal, similar dipping is seen farther to the north beneath the Higher Himalaya [*Schulte-Pelkum et al.*, 2005; *Nabelek et al.*, 2009; *Acton et al.*, 2011]. Our observations are supported by wide-angle seismic reflections along the INDEPTH Tib-1 profile [*Hauck et al.*, 1998] northwest of Bhutan (at around 28°N), which confirm a Moho depth of around 70 km depth in this area within 140 km distance of the southern Himalaya front (Figure 10).

As the extent and geometry of the subducting Indian mantle-slab beneath the Tibetan Plateau affects dynamically the geometry of the Indian Moho by its weight a clear change in the slab geometry is expected. Tomographic results suggest indeed such a change and indicate an abrupt end of the subducting Indian lithosphere beneath the Tibetan Plateau east of 90°E [*Acton et al.*, 2010]. Evidence for an Indian mantle-slab beneath the southeastern Tibetan Plateau so far could not be found [*Li et al.*, 2008], and underthrusting of the Indian lithosphere in eastern Bhutan and Arunachal Pradesh appears to continue only as far north as the IYS (Figure 13). Receiver function results of the Indian Moho in the southeastern Tibetan Plateau by *Shi et al.* [2015] are consistent with these observations and reveal a crustal thickness of only 60 km beneath the Tethyan Himalaya (~28.3°N) at 92°E. In agreement with the almost flat Indian Moho in the southern part of eastern Bhutan, a gentle downbending of the Indian Moho beneath the Higher Himalaya from 50 km depth to around 67 km beneath the Tethyan Himalaya (with less than 10° dip) is only imaged north of 27.7°N [*Shi et al.*, 2015].

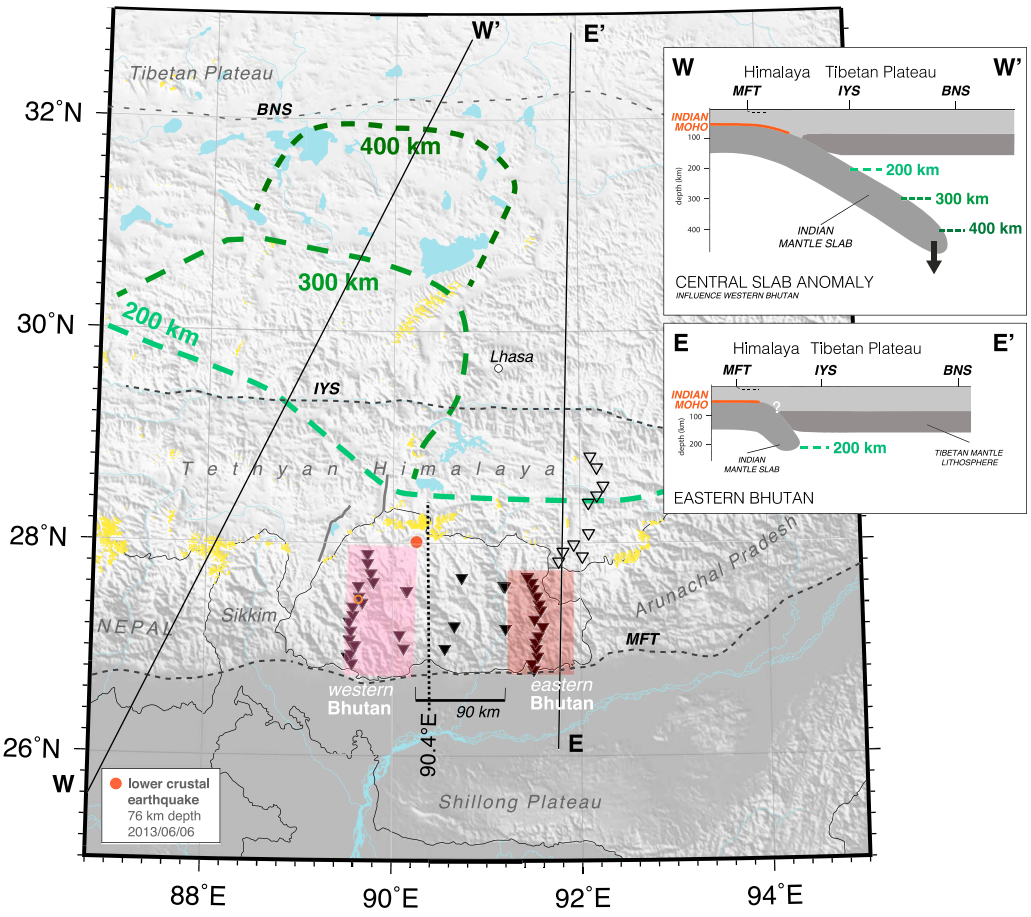

Figure 13. Lithospheric structure of the Indian plate beneath the Eastern Himalaya and the neighboring part of the Tibetan Plateau. The extent of the underthrusting, respectively subducting, Indian plate beneath Tibet is defined by high-velocity anomalies imaged by the teleseismic *P* wave tomography of *Li et al.* [2008, Figures 1 and 7]. Slab contours follow the depth contour lines of the Indian plate inferred by *Li et al.* [2008] and marked by light green, green, and dark green lines. The GANSSER seismic network is shown with solid black triangles and southern stations of the "Gangdese 92°E" seismic array [*Shi et al.*, 2015] are marked as black empty triangle. Epicenter location of a well-constrained lower crustal earthquake (M_L 4.5, 6 June 2013) is shown by the red dot (focal depth 76 ± 1.3 km). The gray thick lines, northwest of Bhutan indicate the location of the wide-angle reflection profiles, Tib-1 and Tib-3 of the INDEPTH project [e.g., *Hauck et al.*, 1998]. Areas with surface elevation higher than 6000 m are indicated in yellow. Red lines in the schematic cross sections WW′ and EE′ indicate the geometry of the Indian Moho derived in this study. Structures are defined as the following: MFT = Main Frontal Thrust, IYS = Indus-Yarlung Suture, and BNS = Bangong-Nujiang Suture. Orange circle in Bhutan indicates the location of Thimphu.

Based on the occurrence of a lower crustal earthquake at 90.2556°E on 6 June 2013 with M_L 4.5 in northwestern Bhutan (Figure 13) with a well-constrained focal depth of about 76 km, we infer a minimum lateral extent of the pronounced downdipping Indian Moho to the east until 90.3°E. Thus, the change in the Indian lithosphere beneath the Himalaya from a northward dipping geometry in the west to an almost flat Moho in the east has to occur within 90 km distance as indicated in Figure 13.

6.2. Collision Structure and Deformation of the Himalaya Orogen in Bhutan

Along the Main Himalayan Thrust (MHT), crustal deformation is assumed to be localized and mechanically decouples the fold-thrust belt of the Himalayan wedge in the south from the underthrusting Indian crust [e.g., *Cattin and Avouac*, 2000; *Lavé and Avouac*, 2000; *Bollinger*, 2004]. In other regions of the Himalaya, the MHT was imaged as a major crustal shear zone first by seismic reflections along the INDEPTH profiles [*Nelson et al.*, 1996; *Hauck et al.*, 1998], and by receiver functions in the Western Himalaya [*Caldwell et al.*, 2013] in central [*Nabelek et al.*, 2009; *Duputel et al.*, 2016], eastern Nepal [*Schulte-Pelkum et al.*, 2005] and indicated in the Sikkim Himalaya [*Acton et al.*, 2011]. Beneath the Lesser Himalaya, it begins as a northward dipping anisotropic

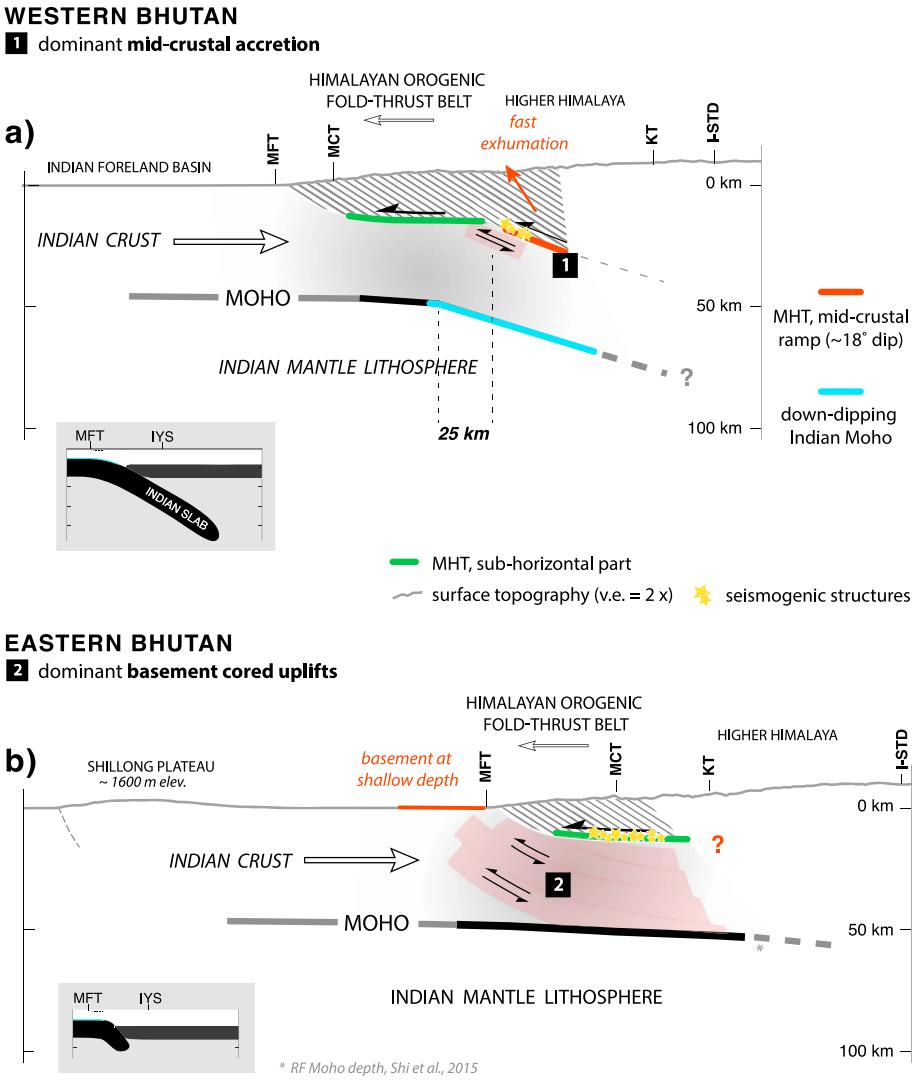

Figure 14. Tectonic models for the involvement of the Indian crust in collision dynamics for eastern and western Bhutan. Hatched area indicates the area of the upper crustal orogenic wedge above the Main Himalayan Thrust (MHT). Main tectonic features mapped at the surface are indicated as the following: MFT = Main Frontal Thrust, MCT = Main Central Thrust, KT = Kakhtang Thrust, and I-STD = inner South Tibetan Detachment. Thick black line represents the Moho geometry defined by our results, and gray lines are extrapolations toward the south and north based on our results and results by *Shi et al.* [2015]. The large-scale lithospheric structure of the underthrusting, respectively, subducting, Indian plate, which affects the collision structure in western and eastern Bhutan, is indicated in the insets. IYS = Indus-Yarlung Suture.

decollement in the upper crust at 8–15 km depth and continues as a middle crustal anisotropic shear zone [*Schulte-Pelkum et al.*, 2005] beneath the Higher Himalaya. Farther to the north, beneath the Tethyan Himalaya in the southern Tibetan Plateau, it seems to reach lower crustal depths [e.g., *Shi et al.*, 2015].

Our receiver function images of the MHT in eastern and western Bhutan support these interpretations of an upper crustal detachment zone at around 12–16 km depth beneath the southern part of the Himalayan orogenic wedge in correlation with a subhorizontal band of seismicity in eastern Bhutan (Figure 14). Similar to *Schulte-Pelkum et al.* [2005], we interpret the upper crustal converter in our results as a subhorizontal shear zone instead of a bulk velocity discontinuity like proposed by *Caldwell et al.* [2013], *Nabelek et al.* [2009], and *Duputel et al.* [2016]. In their models, the conversion signal is associated with low seismic velocities below the MHT, which are caused by trapped fluids released from the underthrusted sediments. However, the occurrence of clustered seismicity associated with this structure in eastern Bhutan points rather to a shear zone with predominantly brittle deformation.

In contrast, the MHT in eastern Bhutan is related to an apparent negative impedance contrast but coincides with a narrow band of subhorizontal seismicity, which is absent in western Bhutan during the operation of the GANSSER network (Figure 14). The local concentration of seismic deformation within few kilometers depth may cause a low-velocity damage zone with specific rheological and anisotropic characteristics, explaining a dominant negative *Ps* phase conversion signal in eastern Bhutan. Evidence for such an influence on the RF signature by repeating seismic slip along a shear zone might be indicated by the correlation of observed clustered seismicity and negative RF converters imaged at upper to middle crustal depth in eastern and western Bhutan (Figures 9 and 12). Although the polarity of the MHT varies in the RF signal between eastern and western Bhutan for its southern subhorizontal part, our results support in general the concept of a main subhorizontal thrust separating the detached Himalayan orogenic wedge from the underthrusting and accreting Indian crust [*Nelson et al.*, 1996; *Hauck et al.*, 1998; *Schulte-Pelkum et al.*, 2005; *Nabelek et al.*, 2009; *Caldwell et al.*, 2013; *Avouac*, 2007].

Toward the north, beneath the southern edge of the Higher Himalaya in western Bhutan and the location of the ramp of the MHT, this intracrustal detachment zone appears to continue at middle crustal depth as indicated by strong intracrustal seismic reflections in the region of the Tethyan Himalaya by the INDEPTH experiment (profile Tib-1) [*Hirn and Sapin*, 1984; *Zhao et al.*, 1993; *Hauck et al.*, 1998]. The reflectivity of the MHT in this part of the orogenic collision is explained by a sharp *P* wave velocity increase with depth [*Hirn and Sapin*, 1984]. A reanalysis of this data by *Zhang and Klemperer* [2010] interpreted this high reflectivity band as the bottom of a low-velocity zone above the MHT caused either by a fluid-rich shear zone or the appearance of partial melt. Both interpretations would be consistent with a positive RF signal caused by an isotropic velocity increase with depth, like we image in the northern part of the western array (Rw in profile WEST 3 in Figure 9). The beginning of this middle crustal ramp of the MHT, however, is characterized by a negative converter and coincide with a cluster of seismicity. Similar to the southern subhorizontal part of the MHT in eastern Bhutan with a distinct concentration of seismicity, we propose that this part of the MHT features an active deformation zone with a particular pattern of shear-induced anisotropy. The change in polarity of this midcrustal converter in correlation with an abrupt ending of the seismicity may mark the transition to ductile deformation along this detachment toward the north as proposed by the locking line of *Vernant et al.* [2014]. The location of the locking line, which is derived from geodetic measurements and defines a change in the deformation type along the MHT, coincides with the change in polarity and the northern end of seismicity. Higher temperatures at this depth could reduce the strength in the anisotropic pattern as proposed by *Mahan* [2006] for the less strong anisotropic signature of the MHT north of eastern Nepal.

6.2.1. Influence of the Middle Crustal Ramp on Upper Crustal Deformation in Bhutan

Thermokinematic models for western Bhutan based on in situ thermochronological ages provide higher long-term exhumation rates at the topographic rise of the Higher Himalaya compared to southern part of the orogenic wedge, where the MHT has a subhorizontal geometry [*Coutand et al.*, 2014]. These locally higher long-term exhumation rates are associated with Neogene crustal exhumation processes from middle crustal depths in association with a middle crustal ramp of the MHT [*Coutand et al.*, 2014]. Such a model correlates well in location and dip with the middle crustal ramp we image with RF (Figure 10). In eastern Bhutan, the location of an apparent middle crustal ramp (Re in profile EAST 1 in Figure 12), either associated with the MHT or not, correlates as well with relatively high exhumation rates in this area derived from zircon (U-Th)/He cooling ages [*Coutand et al.*, 2014]. In addition, the characteristics of this converter with a negative polarity (see previous section) in correlation with a concentration of microseismicity imply an enhanced strain accumulation and active crustal deformation in this part of the orogenic wedge. Active crustal deformation along such a midcrustal ramp would support as well the model of high exhumation rates defined by *Coutand et al.* [2014] and a distinct increase in the average topography from around 3000 m to approximately 4100 m associated with the Higher Himalaya in western Bhutan (Figure 10) and from around 2000 m to 4000 m north of the Kuru Chu Valley in eastern Bhutan.

Previous studies by *Avouac* [2003] and *Bollinger et al.* [2006] in other regions of the Himalaya suggest that this strain accumulation is caused by overthrusting, likely by duplexing [*Avouac*, 2007; *Bollinger et al.*, 2004, 2006], along this middle crustal ramp and provokes the abrupt rise of the Higher Himalaya front with relatively high exhumation rates of middle crustal rocks. For western Bhutan, such a tectonic interpretation would be consistent with our results for the MHT beneath the Higher Himalaya and provides a comprehensive explanation in combination with long-term exhumation rates derived by *Coutand et al.* [2014]. Nevertheless, to sustain the overall long-term growth of the Himalaya orogenic wedge for at least the last 11 Myr, including the

development of duplex structures in the Lesser Himalaya and formation of tectonic windows, like the Tista-Rangit window in Sikkim, Paro window in western, and Kuru Chu half-window in eastern Bhutan [*Coutand et al.*, 2014; *Landry et al.*, 2016], imbrication of material from the underthrusting Indian crust is needed [*Bollinger et al.*, 2006; *Herman et al.*, 2010; *Landry et al.*, 2016].

6.2.2. Involvement of the Underthrusting Indian Crust in the Shortening and Crustal Thickening

Our results reveal additional second-order intracrustal converters in the underthrusting Indian plate. These structures show as well significant lateral variations between eastern and western Bhutan similar to differences in the Indian Moho geometry. We interpret these structures at middle to lower crustal depth as an indication of localized deformation in relation to crustal accretion in the Himalaya, presenting shear or fault zones of several kilometer width with either a shear-induced anisotropic pattern or a contrast in shear velocities (described in sections 5.1 and 5.2).

In other orogens, like the Wind River Mountains in the Sevier and Laramide belts, with an active crustal deformation during the late Cretaceous to Paleogene, seismic reflection data [*Smithson et al.*, 1979] provide clear evidence for a basement-over-sediment thrusting in the upper crust along the Wind River fault. This fault, which dips steeply at the surface, is imaged as a subhorizontal shear zone at middle crustal depth and is interpreted as a localized middle crustal deformation of the cratonic basement [*Schulte-Pelkum and Mahan*, 2014b, 2014a]. *Yonkee and Weil* [2015] described this type of crustal deformation as the evolution of basement-cored uplift or thick-skinned fold-and-thrust tectonics. The thick-skinned fold-and-thrust tectonic model, including an involvement of the underthrusting or subducting plate in crustal thickening and deformation is also proposed for the formations of the Pampeanas in South America [*Jordan and Allmendinger*, 1986; *Ramos et al.*, 2002] or the Taiwan orogen [*Huang et al.*, 2015].

In the eastern part of Bhutan, the occurrence of listric converters of alternating polarity (Figure 14b), particularly well defined in the region of the Kuru Chu half-window, are interpreted here as potential shear or faults zones in the underthrusting Indian crust (see section 5.2). These structures might represent crustal-scale thrust structures pointing to the Himalayan foreland of the Brahmaputra valley similar to the Wind River Thrust. The relatively shallow depth of the sedimentary basin in the south of eastern Bhutan with a narrow width [*Dasgupta et al.*, 2000] can be interpreted as indication of such a basement uplift toward the foreland.

Similar to deformation in the middle and lower crust in the Taiwan orogen and the formation of an anisotropic layer [*Simoes et al.*, 2007], the crustal accretion along those listric bands appears to evolve under ductile shear deformation. Almost no seismicity is observed during the 2 year recording period on the listric-shaped structures (Figure 12). This localized shear deformation is very likely induced by the almost subhorizontal underthrusting of the Indian plate beneath the Himalaya orogenic wedge, extending over 100 km to the north, similar to backstop tectonics in an orogenic collision. The formation of these structures implies a strong involvement of the underthrusting Indian crust in the Himalayan orogeny by accommodating parts of the convergence.

In western Bhutan, we interpret the occurrence of a distinct middle crustal RF structure located beneath the MHT at around 20–30 km depth south of the middle crustal ramp (Cw in profile WEST 1 to WEST 3 in Figure 9) as an intracrustal deformation zone in the underthrusting Indian crust along which crustal slices of the lower to middle crust are stacked on top of each other (description of RF converter in section 5.1). The detachment of crustal material occurs beneath the MHT, south of the present-day middle crustal ramp, and may be involved in the orogenic wedge in a later stage of the collision (Figure 14a). This would imply a southward progression of the middle crustal ramp of the MHT during the evolution of the Himalaya orogen. Such an imbrication of crustal material from the underthrusting Indian crust (footwall) to the orogenic wedge (hanging wall) was proposed by *Bollinger et al.* [2006] and *Grandin et al.* [2012] based on thermochronologic data and the comparison of long-term uplift rates with the interseismic velocity field. In relation to the underthrusting crust, this imbrication appears to occur between the downdip of the Moho and the beginning of the middle crustal ramp of the MHT (Figure 14a). The imbrication is likely to be driven by the shift in kink points of the Moho and the MHT (by approximately 25 km distance) entailing a local increase in crustal thickness of the underthrusting Indian crust. Beneath the southern part of the Himalayan orogenic wedge in western Bhutan brittle deformation in the underthrusting Indian crust appears, as indicated by scattered, middle crustal seismicity (east of 89.7°E, Figures 1 and 10). The lack of distinct middle crustal converters in this area would be consistent with a more scattered seismicity and diffuse deformation pattern in the southern part of western Bhutan.

In correlation with variations in the Moho geometry between eastern and western Bhutan, we explain these differences in the type of crustal accretion in the underthrusting Indian plate by a nonuniform tectonic forcing driven primarily by the large-scale lithospheric structure and dynamics.

7. Conclusions

In this study we introduce a 3-D migration scheme for receiver functions to image the lithospheric structure of the Himalayan collision in Bhutan. Based on a 2-D high-frequency ray approximation in combination with common conversion point (CCP) stacking, we extend the methodology to 3-D including full wavefield characteristics, enhancing of coherent signals by linear phase weighting, and a quality assessment of imaged conversion features. To accurately image dipping conversion structures and to reduce the trade-off between conversion depth and velocity structure, we apply this migration scheme iteratively by updating the velocity structure to the newly derived conversion structure in each iteration. The careful definition of well-resolved areas in the 3-D migration volume based on teleseismic ray coverage rather than on simple hit count allows to reliably resolve lateral variations in the seismic structures which remain often invisible for standard 2-D migration approaches. Furthermore, the proposed migration scheme helps to diminish migration artifacts caused by simplifying assumptions of the velocity structure or ray parameters. Applied to the two GANSSER arrays in Bhutan, we demonstrate that our 3-D migration approach improves the imaging of the lithospheric structure of complex tectonic regions with a limited teleseismic data set even for 2-D arrays.

We image first-order along-strike differences in the lithosphere structure of the Himalayan orogenic collision between western and eastern Bhutan using radial *P*-to-*S* receiver functions. The Moho geometry of the underthrusting Indian plate in eastern Bhutan appears as a subhorizontal converter at a depth of ~50 km. In western Bhutan we image a pronounced northward dip of the Moho north of 27.3°N. This distinct change in the lithospheric structure within only 90 km distance along strike coincides with a change in the large-scale lithosphere structure of the Indian-Eurasian collision inferred by teleseismic tomography [*Li et al.*, 2008]. We associate the distinct downbending of the underthrusting Indian plate in western Bhutan with an attached Indian mantle-slab subducting beneath the Lhasa block (Figure 13) in the north. Toward the east, the influence of the mantle-slab disappears and the underthrusting of the Indian plate is likely to be limited to the Tethyan Himalaya causing a less pronounced crustal thickening beneath the Himalaya and a subhorizontal Moho geometry.

Like in other parts of the Himalaya, we image the Main Himalayan Thrust as a subhorizontal detachment zone between 12 and 16 km depth in the southern part of the Himalaya (Figure 14). During the 2 year observation period most microearthquake activity in eastern Bhutan occurred in the vicinity of this thrust fault system. We also observe clear evidence for intracrustal converters in the underthrusting Indian crust. We interpret these signals as large-scale intracrustal shear zones exhibiting strong anisotropy rather than isotropic velocity contrasts. The location and geometry of these structures provide a strong evidence for significant intracrustal deformation up to crustal imbrication down to the lower crust as a consequence of the involvement of the Indian crust in the orogenic collision process and the long-term growth of the Himalaya. Our results show that these structures vary significantly between western and eastern Bhutan in conformance with the different geometry of the Indian Moho as lower bound of the crustal deformation and are driven by its buoyancy relative to the subducting mantle lithosphere.

Acknowledgments

We thank our colleagues at the Department of Geology and Mines of the Kingdom of Bhutan for the support during the entire fieldwork and the GANSSER fieldwork team. This work benefited from discussions with D. Grujic, and we thank him for his thoughtful comments on the manuscript. We thank N. Rawlinson and M. Sambridge for the possibility to use their Fast Marching Method Code to compute traveltime fields for the 3-D receiver function migration. Constructive reviews by the Associate Editor, Sébastien Chevrot, and two anonymous reviewers helped to improve the manuscript. This work and the deployment of the temporary seismic GANSSER network in Bhutan was funded by the Swiss National Science Foundation (SNF), grant 200021_143467 of G. Hetényi. The new seismic data set recorded by the GANSSER network in 2013 and 2014 is accessible online (http://stations.seddbd.ethz.ch/networks/xa/ or https://doi.org/10.12686/sed/networks/xa) by the end of 2017.

References

Abe, Y., T. Ohkura, K. Hirahara, and T. Shibutani (2011), Common-conversion-point stacking of receiver functions for estimating the geometry of dipping interfaces, *Geophys. J. Int.*, *185*, 1305–1311, doi:10.1111/j.1365-246X.2011.05001.x.

Acton, C. E., K. Priestley, V. K. Gaur, and S. S. Rai (2010), Group velocity tomography of the Indo-Eurasian collision zone, *J. Geophys. Res.*, *115*, B12335, doi:10.1029/2009JB007021.

Acton, C. E., K. Priestley, S. Mitra, and V. K. Gaur (2011), Crustal structure of the Darjeeling-Sikkim Himalaya and southern Tibet, *Geophys. J. Int.*, *184*, 829–852, doi:10.1111/j.1365-246X.2010.04868.x.

Alsdorf, D., et al. (1998a), INDEPTH (International Deep Profiling of Tibet and the Himalaya) multichannel seismic reflection data: Description and availability, *J. Geophys. Res.*, *103*(B11), 26,993–26,999, doi:10.1029/98JB01078.

Alsdorf, D., L. Brown, K. D. Nelson, Y. Makovsky, S. Klemperer, and W. Zhao (1998b), Crustal deformation of the Lhasa terrane, Tibet plateau from Project INDEPTH deep seismic reflection profiles, *Tectonics*, *17*(4), 501–519, doi:10.1029/98TC01315.

Argand, E. (1924), La tectonique de l'Asie. Conférence faite á Bruxelles, le 10 août 1922, Congrès géologique international (XIIIe session)-Belgique 1922, pp. 171–372.

Avouac, J.-P. (2003), Mountain building, erosion, and the seismic cycle in the Nepal Himalaya, *Adv. Geophys.*, *46*, 1–80, doi:10.1016/S0065-2687(03)46001-9.

Avouac, J.-P. (2007), 6.09—Dynamic processes in extensional and compressional settings—Mountain building: From earthquakes to geological deformation, in *Treatise on Geophysics*, edited by G. Schubert, pp. 377–439, Elsevier, Amsterdam, doi:10.1016/B978-044452748-6.00112-7.

Banerjee, P., R. Bürgmann, B. Nagarajan, and E. Apel (2008), Intraplate deformation of the Indian subcontinent, *Geophys. Res. Lett.*, *35*, L18301, doi:10.1029/2008GL035468.

Bianchi, I., J. Park, P. N. Agostinetti, and V. Levin (2010), Mapping seismic anisotropy using harmonic decomposition of receiver functions: An application to Northern Apennines, Italy, *J. Geophys. Res.*, *115*, B12317, doi:10.1029/2009JB007061.

Bilham, R., and P. England (2001), Plateau "pop-up" in the great 1897 Assam earthquake, *Nature*, *410*(6830), 806–809, doi:10.1038/35071057.

Biswas, S., I. Coutand, D. Grujic, C. Hager, D. Stöckli, and B. Grasemann (2007), Exhumation and uplift of the Shillong plateau and its influence on the eastern Himalayas: New constraints from apatite and zircon (U-Th-[Sm])/He and apatite fission track analyses, *Tectonics*, *26*, TC6013, doi:10.1029/2007TC002125.

Bollinger, L. (2004), Stress buildup in the Himalaya, *J. Geophys. Res.*, *109*, B11405, doi:10.1029/2003JB002911.

Bollinger, L., J. Avouac, O. Beyssac, E. Catlos, T. Harrison, M. Grove, B. Goffé, and S. Sapkota (2004), Thermal structure and exhumation history of the Lesser Himalaya in central Nepal, *Tectonics*, *23*, TC5015, doi:10.1029/2003TC001564.

Bollinger, L., P. Henry, and J. Avouac (2006), Mountain building in the Nepal Himalaya: Thermal and kinematic model, *Earth Planet. Sci. Lett.*, *244*, 58–71, doi:10.1016/j.epsl.2006.01.045.

Bostock, M., S. Rondenay, and J. Shragge (2001), Multiparameter two-dimensional inversion of scattered teleseismic body waves: 1. Theory for oblique incidence, *J. Geophys. Res.*, *106*, 30,771–30,782, doi:10.1029/2001JB000330.

Bostock, M. G., and S. Rondenay (1999), Migration of scattered teleseismic body waves, *Geophys. J. Int.*, *137*, 732–746, doi:10.1046/j.1365-246x.1999.00813.x.

Caldwell, W. B., S. L. Klemperer, J. F. Lawrence, S. S. Rai, and Ashish (2013), Characterizing the Main Himalayan Thrust in the Garhwal Himalaya, India with receiver function CCP stacking, *Earth Planet. Sci. Lett.*, *367*, 15–27, doi:10.1016/j.epsl.2013.02.009.

Cassidy, J. (1992), Numerical experiments in broadband receiver function analysis, *Bull. Seismol. Soc. Am.*, *82*(3), 1453–1474.

Cattin, R., and J. P. Avouac (2000), Modeling mountain building and the seismic cycle in the Himalaya of Nepal, *J. Geophys. Res.*, *105*(B6), 13,389–13,407, doi:10.1029/2000JB900032.

Červený, V., and J. E. P. Soares (1992), Fresnel volume ray tracing, *Geophysics*, *57*(7), 902–915, doi:10.1190/1.1443303.

Clark, M. K., and R. Bilham (2008), Miocene rise of the Shillong Plateau and the beginning of the end for the Eastern Himalaya, *Earth Planet. Sci. Lett.*, *269*(3–4), 337–351, doi:10.1016/j.epsl.2008.01.045.

Clouser, R. H., and C. A. Langston (1995), Effect of sinusoidal interfaces on teleseismic *P*-wave receiver functions, *Geophys. J. Int.*, *123*(2), 541–558, doi:10.1111/j.1365-246X.1995.tb06870.x.

Coutand, I., D. M. Whipp, D. Grujic, M. Bernet, M. G. Fellin, B. Bookhagen, K. R. Landry, S. K. Ghalley, and C. Duncan (2014), Geometry and kinematics of the Main Himalayan Thrust and Neogene crustal exhumation in the Bhutanese Himalaya derived from inversion of multithermochronologic data, *J. Geophys. Res. Solid Earth*, *119*, 1446–1481, doi:10.1002/2013JB010891.

Daniel, C. G., L. S. Hollister, R. R. Parrish, and D. Grujic (2003), Exhumation of the main central thrust from lower crustal depths, Eastern Bhutan Himalaya, *J. Metamorph. Geol.*, *21*(4), 317–334, doi:10.1046/j.1525-1314.2003.00445.x.

Dasgupta, S., P. Narula, S. Acharyya, and J. Banerjee (2000), *Seismotectonic Atlas of India and its Environs*, Geol. Surv. of India, Bangalore, India.

DeCelles, P. G., D. M. Robinson, J. Quade, T. P. Ojha, C. N. Garzione, P. Copeland, and B. N. Upreti (2001), Stratigraphy, structure, and tectonic evolution of the Himalayan fold-thrust belt in western Nepal, *Tectonics*, *20*(4), 487–509, doi:10.1029/2000TC001226.

Dueker, K. G., and A. F. Sheehan (1997), Mantle discontinuity structure from midpoint stacks of converted *P* to *S* waves across the Yellowstone hotspot track, *J. Geophys. Res.*, *102*, 8313–8327.

Dueker, K. G., and A. F. Sheehan (1998), Mantle discontinuity structure beneath the Colorado Rocky Mountains and High Plains, *J. Geophys. Res.*, *103*, 7153–7169, doi:10.1029/97JB03509.

Duputel, Z., J. Vergne, L. Rivera, G. Wittlinger, V. Farra, and G. Hetényi (2016), The 2015 Gorkha earthquake: A large event illuminating the Main Himalayan Thrust fault, *Geophys. Res. Lett.*, *43*, 2517–2525, doi:10.1002/2016GL068083.

Frassetto, A., G. Zandt, H. Gilbert, T. Owens, and C. Jones (2010), Improved imaging with phase-weighted common conversion point stacks of receiver functions, *Geophys. J. Int.*, *182*(1), 368–374, doi:10.1111/j.1365-246X.2010.04617.x.

Gahalaut, V., S. Rajput, and B. Kundu (2011), Low seismicity in the Bhutan Himalaya and the stress shadow of the 1897 Shillong Plateau earthquake, *Phys. Earth Planet. Inter.*, *186*, 97–102, doi:10.1016/j.pepi.2011.04.009.

Gansser, A. (1964), *Geology of the Himalayas*, Interscience, 289 pp., New York.

Gansser, A. (1983), *Geology of the Bhutan Himalaya*, Birkhauser Verlag, Basel, Switz.

Grandin, R., M.-P. Doin, L. Bollinger, B. Pinel-Puysségur, G. Ducret, R. Jolivet, and S. N. Sapkota (2012), Long-term growth of the Himalaya inferred from interseismic InSAR measurement, *Geology*, *40*(12), 1059–1062, doi:10.1130/G33154.1.

Guo, Z., X. Gao, H. Yao, J. Li, and W. Wang (2009), Midcrustal low-velocity layer beneath the central Himalaya and southern Tibet revealed by ambient noise array tomography, *Geochem. Geophys. Geosyst.*, *10*, Q05007, doi:10.1029/2009GC002458.

Hauck, M. L., K. D. Nelson, L. D. Brown, W. Zhao, and A. R. Ross (1998), Crustal structure of the Himalayan orogen at ~90° east longitude from Project INDEPTH deep reflection profiles, *Tectonics*, *17*(4), 481–500, doi:10.1029/98TC01314.

Herman, F., et al. (2010), Exhumation, crustal deformation, and thermal structure of the Nepal Himalaya derived from the inversion of thermochronological and thermobarometric data and modeling of the topography, *J. Geophys. Res.*, *115*, B06407, doi:10.1029/2008JB006126.

Hetényi, G., Y. Ren, B. D. Dando, G. W. Stuart, E. Hegedűs, A. C. Kovács, and G. A. Houseman (2015), Crustal structure of the Pannonian Basin: The AlCaPa and Tisza Terrains and the Mid-Hungarian Zone, *Tectonophysics*, *646*, 106–116, doi:10.1016/j.tecto.2015.02.004.

Hirn, A., and M. Sapin (1984), The Himalayan zone of crustal interaction: Suggestions from explosion seismology, *Ann. Geophys.*, *2*, 123–130.

Hirschmiller, J., D. Grujic, B. Bookhagen, I. Coutand, P. Huyghe, J. L. Mugnier, and T. Ojha (2014), What controls the growth of the Himalayan foreland fold-and-thrust belt?, *Geology*, *42*, 247–250, doi:10.1130/G35057.1.

Huang, G. D., F. T. Wu, S. W. Roecker, and A. F. Sheehan (2009), Lithospheric structure of the central Himalaya from 3-D tomographic imaging, *Tectonophysics*, *475*, 524–543, doi:10.1016/j.tecto.2009.06.023.

Huang, T.-Y., Y. Gung, B.-Y. Kuo, L.-Y. Chiao, and Y.-N. Chen (2015), Layered deformation in the Taiwan orogen, *Science*, *349*(6249), 720–723, doi:10.1126/science.aab1879.

Hung, S.-H., W.-P. Chen, and L.-Y. Chiao (2011), A data-adaptive, multiscale approach of finite-frequency, traveltime tomography with special reference to *P* and *S* wave data from central Tibet, *J. Geophys. Res.*, *116*, B06307, doi:10.1029/2010JB008190.

Husen, S., and E. Kissling (2001), Local earthquake tomography between rays and waves: Fat ray tomography, *Phys. Earth Planet. Inter.*, *123*, 127–147, doi:10.1016/S0031-9201(00)00206-5.

Jordan, T. E., and R. W. Allmendinger (1986), The Sierras Pampeanas of Argentina: A modern analogue of Rocky Mountain foreland deformation, *Am. J. Sci.*, *286*(10), 737–764.

Kellett, D., D. Grujic, and S. Erdmann (2009), Miocene structural reorganization of the South Tibetan detachment, eastern Himalaya: Implications for continental collision, *Lithosphere*, *1*(5), 259–281.

Kennett, B. L. N., and E. R. Engdahl (1991), Traveltimes for global earthquake location and phase identification, *Geophys. J. Int.*, *105*(2), 429–465, doi:10.1111/j.1365-246X.1991.tb06724.x.

Kissling, E. (1988), Geotomography with local earthquake data, *Rev. Geophys.*, *26*, 659–698, doi:10.1029/RG026i004p00659.

Kool, D. M., N. Rawlinson, and M. Sambridge (2006), A practical grid based method for tracking multiple refraction and reflection phases in threeŘ dimensional heterogeneous media, *Geophys. J. Int.*, *167*, 253–270, doi:10.1111/j.1365-246X.2006.03078.x.

Kosarev, G. (1999), Seismic evidence for a detached Indian lithospheric mantle beneath Tibet, *Science*, *283*, 1306–1309, doi:10.1126/science.283.5406.1306.

Landry, K. R., I. Coutand, D. M. Whipp, D. Grujic, and J. K. Hourigan (2016), Late neogene tectonically driven crustal exhumation of the Sikkim Himalaya: Insights from inversion of multithermochronologic data, *Tectonics*, *35*, 833–859, doi:10.1002/2015TC004102.

Langston, C. A. (1977), The effect of planar dipping structure on source and receiver responses for constant ray parameter, *Bull. Seismol. Soc. Am.*, *67*(4), 1029–1050.

Lavé, J., and J. P. Avouac (2000), Active folding of fluvial terraces across the Siwaliks Hills, Himalayas of central Nepal, *J. Geophys. Res.*, *105*(B3), 5735–5770, doi:10.1029/1999JB900292.

Levander, A., F. Niu, and W. W. Symes (2013), Imaging teleseismic *P* to *S* scattered waves using the kirchhoff integral, in *Seismic Earth: Array Analysis of Broadband Seismograms*, edited by A. Levander and G. Nolet, pp. 149–169, AGU, Washington, D. C., doi:10.1029/157GM10

Levin, V., and J. Park (1997), *P-SH* conversions in a flat-layered medium with anisotropy of arbitrary orientation, *Geophys. J. Int.*, *131*(2), 253–266, doi:10.1111/j.1365-246X.1997.tb01220.x.

Levin, V., and J. Park (1998), *P-SH* conversions in layered media with hexagonally symmetric anisotropy: A cookbook, in *Geodynamics of Lithosphere and Earth's Mantle: Seismic Anisotropy as a Record of the Past and Present Dynamic Processes*, edited by J. Plomerova, R. C. Liebermann, and V. Babuska, pp. 669–697, Birkhauser, Basel, Switz., doi:10.1007/978-3-0348-8777-9_25.

Li, C., R. D. van der Hilst, A. S. Meltzer, and E. R. Engdahl (2008), Subduction of the Indian lithosphere beneath the Tibetan Plateau and Burma, *Earth Planet. Sci. Lett.*, *274*(1–2), 157–168, doi:10.1016/j.epsl.2008.07.016.

Liang, X., Y. Shen, Y. J. Chen, and Y. Ren (2011), Crustal and mantle velocity models of southern Tibet from finite frequency tomography, *J. Geophys. Res.*, *116*, B02408, doi:10.1029/2009JB007159.

Ligorría, J. P., and C. J. Ammon (1999), Iterative deconvolution and receiver-function estimation, *Bull. Seismol. Soc. Am.*, *89*(5), 1395–1400.

Long, S., N. McQuarrie, T. Tobgay, and D. Grujic (2011a), Geometry and crustal shortening of the Himalayan fold-thrust belt, eastern and central Bhutan, *Geol. Soc. Am. Bull.*, *123*(7–8), 1427–1447, doi:10.1130/B30203.1.

Long, S., N. McQuarrie, T. Tobgay, D. Grujic, and L. Hollister (2011b), Geologic map of Bhutan, *J. Maps*, *7*, 184–192, doi:10.4113/jom.2011.1159.

Mahan, K. (2006), Retrograde mica in deep crustal granulites: Implications for crustal seismic anisotropy, *Geophys. Res. Lett.*, *33*, L24301, doi:10.1029/2006GL028130.

Miller, D., M. Oristaglio, and G. Beylkin (1987), A new slant on seismic imaging: Migration and integral geometry, *Geophysics*, *52*(7), 943–964, doi:10.1190/1.1442364.

Mitra, S., K. Priestley, A. K. Bhattacharyya, and V. K. Gaur (2004), Crustal structure and earthquake focal depths beneath northeastern India and southern Tibet, *Geophys. J. Int.*, *160*, 227–248, doi:10.1111/j.1365-246X.2004.02470.x.

Monsalve, G., A. Sheehan, C. Rowe, and S. Rajaure (2008), Seismic structure of the crust and the upper mantle beneath the Himalayas: Evidence for eclogitization of lower crustal rocks in the Indian plate, *J. Geophys. Res.*, *113*, B08315, doi:10.1029/2007JB005424.

Nabelek, J., G. Hetenyi, J. Vergne, S. Sapkota, B. Kafle, M. Jiang, H. Su, J. Chen, B. Huang, and The Hi-CLIMB Team (2009), Underplating in the Himalaya-Tibet collision zone revealed by the Hi-CLIMB experiment, *Science*, *325*, 1371–1374, doi:10.1126/science.1167719.

Najman, Y., L. Bracciali, R. R. Parrish, E. Chisty, and A. Copley (2016), Evolving strain partitioning in the Eastern Himalaya: The growth of the Shillong Plateau, *Earth Planet. Sci. Lett.*, *433*, 1–9, doi:10.1016/j.epsl.2015.10.017.

Nelson, K. D., et al. (1996), Partially molten middle crust beneath southern Tibet: Synthesis of project INDEPTH results, *Science*, *274*(5293), 1684–1688, doi:10.1126/science.274.5293.1684.

Ramos, V. A., E. Cristallini, and D. J. Perez (2002), The Pampean flat-slab of the Central Andes, *J. South Am. Earth Sci.*, *15*(1), 59–78, doi:10.1016/S0895-9811(02)00006-8.

Rawlinson, N., and M. Sambridge (2004), Wave front evolution in strongly heterogeneous layered media using the fast marching method, *Geophys. J. Int.*, *156*, 631–647, doi:10.1111/j.1365-246X.2004.02153.x.

Rondenay, S., M. G. Bostock, and K. M. Fischer (2005), Multichannel inversion of scattered teleseismic body waves: Practical considerations and applicability, in *Seismic Earth: Array Analysis of Broadband Seismograms, Geophys. Monogr. Ser.*, vol. 157, edited by A. Levander and G. Nolet, pp. 187–203, AGU, Washington, D. C.

Rychert, C. A., S. Rondenay, and K. M. Fischer (2007), *P* to *S* and *S* to *P* imaging of a sharp lithosphere asthenosphere boundary beneath eastern North America, *J. Geophys. Res.*, *112*, B08314, doi:10.1029/2006JB004619.

Schelling, D., and K. Arita (1991), Thrust tectonics, crustal shortening, and the structure of the far-eastern Nepal Himalaya, *Tectonics*, *10*(5), 851–862, doi:10.1029/91TC01011.

Schimmel, M., and H. Paulssen (1997), Noise reduction and detection of weak, coherent signals through phase-weighted stacks, *Geophys. J. Int.*, *130*, 497–505, doi:10.1111/j.1365-246X.1997.tb05664.x.

Schulte-Pelkum, V., and K. H. Mahan (2014a), Imaging faults and shear zones using receiver functions, *Pure Appl. Geophys.*, *171*(11), 2967–2991, doi:10.1007/s00024-014-0853-4.

Schulte-Pelkum, V., and K. H. Mahan (2014b), A method for mapping crustal deformation and anisotropy with receiver functions and first results from USArray, *Earth Planet. Sci. Lett.*, *402*, 221–233, doi:10.1016/j.epsl.2014.01.050.

Schulte-Pelkum, V., G. Monsalve, A. Sheehan, M. Pandey, S. Sapkota, R. Bilham, and F. Wu (2005), Imaging the Indian subcontinent beneath the Himalaya, *Nature*, *435*(7046), 1222–1225, doi:10.1038/nature03678.

Sheehan, A. F., T. L. de la Torre, G. Monsalve, G. A. Abers, and B. R. Hacker (2014), Physical state of Himalayan crust and uppermost mantle: Constraints from seismic attenuation and velocity tomography, *J. Geophys. Res. Solid Earth*, *119*, 567–580, doi:10.1002/2013JB010601.

Sherrington, H. F., G. Zandt, and A. Frederiksen (2004), Crustal fabric in the Tibetan Plateau based on waveform inversions for seismic anisotropy parameters, *J. Geophys. Res.*, *109*, B02312, doi:10.1029/2002JB002345.

Shi, D., Z. Wu, S. L. Klemperer, W. Zhao, G. Xue, and H. Su (2015), Receiver function imaging of crustal suture, steep subduction, and mantle wedge in the eastern India–Tibet continental collision zone, *Earth Planet. Sci. Lett.*, *414*, 6–15, doi:10.1016/j.epsl.2014.12.055.

Simoes, M., J. P. Avouac, O. Beyssac, B. Goffé, K. A. Farley, and Y.-G. Chen (2007), Mountain building in Taiwan: A thermokinematic model, *J. Geophys. Res.*, *112*, B11405, doi:10.1029/2006JB004824.

Singh, A., R. M. Kumar, and S. P. Raju (2010), Seismic structure of the underthrusting Indian crust in Sikkim Himalaya, *Tectonics*, *29*, TC6021, doi:10.1029/2010TC002722.

Smithson, S. B., J. A. Brewer, S. Kaufman, J. E. Oliver, and C. A. Hurich (1979), Structure of the Laramide Wind River Uplift, Wyoming, from COCORP deep reflection data and from gravity data, *J. Geophys. Res.*, *84*(B11), 5955–5972, doi:10.1029/JB084iB11p05955.

Spada, M., I. Bianchi, E. Kissling, N. P. Agostinetti, and S. Wiemer (2013), Combining controlled-source seismology and receiver function information to derive 3-D Moho topography for Italy, *Geophys. J. Int.*, *194*, 1050–1068, doi:10.1093/gji/ggt148.

Tobgay, T., N. McQuarrie, S. Long, M. J. Kohn, and S. L. Corrie (2012), The age and rate of displacement along the Main Central Thrust in the western Bhutan Himalaya, *Earth Planet. Sci. Lett.*, *319–320*, 146–158, doi:10.1016/j.epsl.2011.12.005.

van der Beek, P., C. Litty, M. Baudin, J. Mercier, X. Robert, and E. Hardwick (2016), Contrasting tectonically driven exhumation and incision patterns, western versus central Nepal Himalaya, *Geology*, *44*(4), 327–330.

Vernant, P., R. Bilham, W. Szeliga, D. Drupka, S. Kalita, A. K. Bhattacharyya, V. K. Gaur, P. Pelgay, R. Cattin, and T. Berthet (2014), Clockwise rotation of the Brahmaputra Valley relative to India: Tectonic convergence in the eastern Himalaya, Naga Hills, and Shillong Plateau, *J. Geophys. Res. Solid Earth*, *119*, 6558–6571, doi:10.1002/2014JB011196.

Yilmaz, Ö. (2001), Seismic data analysis,Soc. Explor. Geophys., Tulsa, Okla., doi:10.1190/1.9781560801580.

Yonkee, W. A., and A. B. Weil (2015), Tectonic evolution of the Sevier and Laramide belts within the North American Cordillera orogenic system, *Earth Sci. Rev.*, *150*, 531–593, doi:10.1016/j.earscirev.2015.08.001.

Zhang, Z., and S. Klemperer (2010), Crustal structure of the Tethyan Himalaya, southern Tibet: New constraints from old wide-angle seismic data, *Geophys. J. Int.*, *181*(3), 1247–1260, doi:10.1111/j.1365-246X.2010.04578.x.

Zhao, W. (2011), Tibetan plate overriding the Asian plate in central and northern Tibet, *Nat. Geosci.*, *4*, 870–873, doi:10.1038/ngeo1309.

Zhao, W., K. D. Nelson, J. Che, J. Quo, D. Lu, C. Wu, and X. Liu (1993), Deep seismic reflection evidence for continental underthrusting beneath southern Tibet, *Nature*, *366*(6455), 557–559.

Zhu, L., and H. Kanamori (2000), Moho depth variation in Southern California from teleseismic receiver functions, *J. Geophys. Res.*, *105*, 2969–2980, doi:10.1029/1999JB900322.